

Instabilities and bifurcations of liquid films flowing down a rotating fibre

Rong Liu¹ and Zijing Ding^{2,3,†}

¹School of Mechanical and Electrical Engineering, Gui Lin University of Electronic Technology, Gui Lin 541004, PR China

²School of Energy Science and Engineering, Harbin Institute of Technology, Harbin 150001, PR China

³Department of Applied Mathematics and Theoretical Physics, University of Cambridge, Wilberforce Road, Cambridge CB3 0WA, UK

(Received 5 September 2019; revised 19 April 2020; accepted 29 May 2020)

We consider the dynamics of a gravity-driven flow coating a vertical fibre rotating about its axis. This flow exhibits rich dynamics including the formation of bead-like structures and different types of steady or oscillatory travelling waves driven by a Rayleigh–Plateau mechanism modified by the presence of gravity and rotation. Linear stability shows that the axisymmetric mode dominates the instability when the rotation is slow, which allows us to derive a two-dimensional model equation under the long-wave assumption. The spatio-temporal dynamics and nonlinear wave solutions are then investigated by the model equation. The spatio-temporal stability analysis showed that the absolute instability is enhanced by the rotation. Steady travelling-wave states and relative periodic states are observed in the numerical simulations of the model equation, which show that the rotation tends to suppress the formation of relative periodic states. To examine this, a linear stability analysis of steady travelling waves is performed, indicating that the rotation has a stabilizing effect on the steady travelling waves. This result is adverse to the destabilizing effect of rotation on the linear stability of initially uniform films. A bifurcation analysis shows that the relative periodic state is born from the instability of steady travelling wave, which represents the coalescence and breakup process between a large droplet and a serial of much smaller droplets.

Key words: thin films, coating

1. Introduction

The coating of liquid film on a fibre has given rise to considerable scientific interest because of its relevance to many industrial applications, for example, draining, coating of insulation on a wire, and the protection of tube walls (Quéré 1999). The exterior coating flow driven by gravity down a vertical fibre is a typical unstable open flow in which

† Email address for correspondence: z.ding@hit.edu.cn

formation of droplets, or beads, due to the well-known Rayleigh–Plateau mechanism (Rayleigh 1892) inevitably occurs.

Two different types of instabilities emerge in the exterior coating flows. One is the classical spatio-temporal disorder induced by the Kapitza instability mode (Kapitza & Kapitza 1949) of films falling down vertical planes, hereinafter referred to as ‘K’ mode. The wavy dynamics on a liquid film flow down an inclined or vertical plate has given rise to considerable interest up to date. For more related works to the dynamics of a falling film on inclined plate, we refer the readers to the monograph by Kalliadasis *et al.* (2012). The other type is the emergence of very regular drop-like wave patterns due to the Rayleigh–Plateau instability, hereinafter referred to as ‘RP’ mode (Kliakhandler, Davis & Bankoff 2001; Craster & Matar 2006).

Quéré (1990) was the first to perform experiments to investigate the drop formation in the process of drawing wires from liquid baths. He found that for a thick film on a slender fibre, small undulations grow into large droplets by swallowing the other ones, and quickly fall, leaving behind them a thick film which breaks into droplets. However, for a thin film on a thick fibre, the process of drop formation may be arrested by the mean flow.

The problems of the dynamics of exterior coating flows on fibres have been extensively investigated using asymptotic models. Frenkel (1992) derived a thin film model using a lubrication approximation for the coating flow wherein the fibre radius a is assumed to be much larger than the film thickness h . Kalliadasis & Chang (1994) studied the mechanism for drop formation of the problem using Frenkel’s equation, and found that when the thickness of the coating film exceeds a critical thickness h_c , the interface can evolve into highly localized drops due to the Rayleigh–Plateau mechanism. Kliakhandler *et al.* (2001) performed experiments to examine the drop formation process in the case where the film thicknesses are of the order of the fibre radii. Instead of using Frenkel’s thin film model, a thick film model was proposed by Kliakhandler *et al.* (2001). Note that the thick film model is not asymptotically consistent, which was addressed by Craster & Matar (2006). The modelling work mentioned above neglects inertia effects. Therefore, these models are only valid for small Reynolds numbers of $Re \sim O(1)$ and cannot account for the ‘K’ hydrodynamic instability mechanism. Ruyer-Quil *et al.* (2008) took into account inertia and streamwise viscous diffusion and formulated two coupled evolution equations for both the film thickness and volumetric flow rate. This model is valid for moderate Reynolds numbers, both small and $O(1)$ aspect ratios of h/a .

Instability characteristics in films can be categorized by the location where instability growth can be visually detected. Transitions between different wave regimes in coating flows can be understood by the concept of the absolute (AI) and convective instabilities (CI) which was first developed in the field of plasma physics (Briggs 1964; Bers 1975) and later extended to the problems of fluid mechanics (Huerre & Monkewitz 1990). In the laboratory frame of reference, the instability is said to be convective if the disturbance is advected and eventually dies out if it is not sustained continuously at a fixed point. On the contrary, absolutely unstable flows display an intrinsic self-sustaining feature: the perturbation is so strongly amplified that it contaminates the entire flow region. Duprat *et al.* (2007) have studied both experimentally and theoretically the absolute and convective stabilities for a viscous film flowing down a vertical fibre. The result showed that at large or small film thicknesses, the instability is convective. Whereas, the ‘RP’ mode may trigger an absolute instability in an intermediate range of film thicknesses when the fibre radius is sufficiently small.

Recently, the problems of coating flows arising in more complex situations, for example in the presence of thermocapillarity (Liu & Liu 2014), subject to electric field (Ding & Willis 2019), in contact with countercurrent gas flow (Dietze & Ruyer-Quil 2015),

flowing over a slippery surface (Halpern & Wei 2017; Ji *et al.* 2019), have been extensively investigated due to their relevance to technological applications. Except for the attempts in the complex situations mentioned above, rotation is an effective way to control the stability and dynamics of coating flows. The coating flow outside or inside a rotating cylinder arises in many industrial applications owing to the need to control, protect and functionalize surfaces (Ruschak & Scriven 1976; Moffatt 1977; Ashmore & Hosoi 2003). Dynamics of a viscous film on the outer surface of a horizontal rotating cylinder was first studied by Moffatt (1977). The flow of a liquid layer around the inside surface of a rotating horizontal drum or cylinder, referred to as the rimming flow, has been extensively investigated experimentally and numerically. Many interesting effects, including two-dimensional steady states (Ruschak & Scriven 1976; Johnson 1988), three-dimensional instabilities and time-periodic flows (Thoroddsen & Mahadevan 1997; Hosoi & Mahadevan 1999) and the effect of surface tension (Pougatch & Frigaard 2011; Benilov & Lapin 2013; Groh & Kelmanson 2014) have been represented in the literature.

The works related to the coating flow or rimming flow over a rotating cylindrical substrate mentioned above focus on the case of horizontally placed cylinders. However, a careful look at the present literature indicates that the works on the coating flows on a vertical rotating cylinder are very limited. Dávalos-Orozco & Ruiz-Chavarría (1993) studied the linear stability of a fluid layer flowing down the inside and outside of a rotating vertical cylinder. Two additional approximations, i.e. the small wavenumber and the small Reynolds number, are made in their analysis. The result showed that for flow outside the cylinder, the centrifugal force may trigger the non-axisymmetric with the azimuthal wavenumber $m = 1$ as the dominant mode of instability. The work by Dávalos-Orozco & Ruiz-Chavarría (1993) work does not apply to the nonlinear regime of the problem. Chen, Chen & Yang (2004) investigated the stability of a condensate film on the outer surface of a rotating cylinder in the framework of the lubrication approximation and showed that the effect of increasing rotational speed is destabilizing. Rietz *et al.* (2017) experimentally investigated the evolution of a thin film on the outside of a vertical rotating cylinder of large radius. The experimental results indicated that the Rayleigh–Taylor instability induced by destabilizing body force result in the emergence of rivulets. Directly after destabilization of two-dimensional waves into rivulets, detachment of droplets from the cylinder has been observed.

For the coating flows on a cylinder, three different nonlinear flow regimes were observed in experimental studies, depending on the flow rates, when the fibre is stationary (Kliakhandler *et al.* 2001), which were labelled flow regime ‘a’, ‘b’ and ‘c’. Flow regime ‘a’ consists of long-spaced big droplets, which can be represented by a steady travelling-wave solution (Craster & Matar 2006). Flow regime ‘b’ is a necklace-like structure – close and regularly spaced droplets, which cannot be described by the long-wave model. Flow regime ‘c’ is a time-dependent flow, in which a big droplet coexists with several small droplets. Very recently, Ding & Willis (2019) used a relative periodic solution to describe the flow regime ‘c’, which showed a very similar dynamics to the experimental observation. However, it remains unknown that how the rotation influences the nonlinear dynamics, i.e. steady travelling-wave solutions (Craster & Matar 2006) and relative periodic solutions (Ding & Willis 2019), which will be explored in the present study.

In the present work, we consider the problem of a gravity-driven coating flow outside a vertical rotating fibre. Firstly, we will perform a linear stability analysis of the Navier–Stokes equations and examine the stabilities of axisymmetric and non-axisymmetric disturbances. The linear stability analysis demonstrates that the Coriolis effect is negligible for the physical parameters considered in the present system.

We investigated the effect of rotation on the stability of the most unstable mode. At low frequency of rotation, the most unstable mode is in the form of axisymmetric disturbance. For axisymmetric cases, neglecting the Coriolis effect allows us to derive a long-wave model, which is valid for both thin and thick films. To validate the long wave model, we compare the linear stability analysis of the long-wave model with the linear stability analysis of the Navier–Stokes equations. Further, the nonlinear evolution of the long-wave model for the axisymmetric case is compared with the results of direct numerical simulation (DNS). At high frequency of rotation, the most unstable mode is achieved by streamwise uniform and non-axisymmetric disturbance. In this case, no asymptotic model can be obtained for thick films. We studied the nonlinear evolution for non-axisymmetric disturbance by DNS in the appendices.

The rest of the present paper is organized as follows. In § 2 the mathematical formulation of the physical model is presented. The linear stability analysis of the three-dimensional (3-D) problem of the Navier–Stokes equations is performed to evaluate the contribution of Coriolis forces and to examine the most unstable mode for various rotation frequencies. Further, the evolution equation is derived in the framework of long-wave approximation for the axisymmetric problem. In § 3 we study the linear stability of the long-wave problem. The effect of rotation on the time growth rate and frequency of the disturbance is studied by a temporal stability analysis. A spatio-temporal stability analysis is performed to examine the characteristics of absolute and convective instabilities. In § 4, we investigate the travelling-wave solutions and their instabilities. The simulation of travelling waves perturbed by the small disturbance shows that the travelling wave loses stability to a ‘relative’ periodic solution. Using a bifurcation analysis with branch continuation, the relative periodic solutions are tracked as parameter changes. In § 6, conclusions are provided.

2. Mathematical formulation

As shown in figure 1, a Newtonian fluid, of dynamic viscosity μ and density ρ , flows down a vertical fibre of radius $r = a$ under gravity g . The cylinder rotates about its axis (z -axis) at an angular speed Ω . The initial radius of the fluid ring measured from the centre of the fibre is $r = R$. Let (r, θ, z) be the rotating cylindrical coordinates moving with the fibre.

The dynamics of the flow are governed by the Navier–Stokes equations,

$$\partial_r u + \frac{u}{r} + \frac{\partial_\theta v}{r} + \partial_z w = 0, \tag{2.1}$$

$$\begin{aligned} &\partial_t u + u\partial_r u + \frac{v}{r}\partial_\theta u + w\partial_z u - \frac{v^2}{r} \\ &= -\frac{\partial_r p}{\rho} + \Omega^2 r - 2\Omega v + \frac{\mu}{\rho} \left[\partial_{rr} u + \frac{\partial_r u}{r} + \frac{\partial_{\theta\theta} u}{r^2} + \partial_{zz} u - \frac{u}{r^2} - \frac{2}{r^2} \partial_\theta v \right], \end{aligned} \tag{2.2}$$

$$\begin{aligned} &\partial_t v + u\partial_r v + \frac{v}{r}\partial_\theta v + w\partial_z v + \frac{uv}{r} \\ &= -\frac{1}{\rho} \frac{\partial_\theta p}{r} + 2\Omega u + \frac{\mu}{\rho} \left[\partial_{rr} v + \frac{\partial_r v}{r} + \frac{\partial_{\theta\theta} v}{r^2} + \partial_{zz} v - \frac{v}{r^2} + \frac{2}{r^2} \partial_\theta u \right], \end{aligned} \tag{2.3}$$

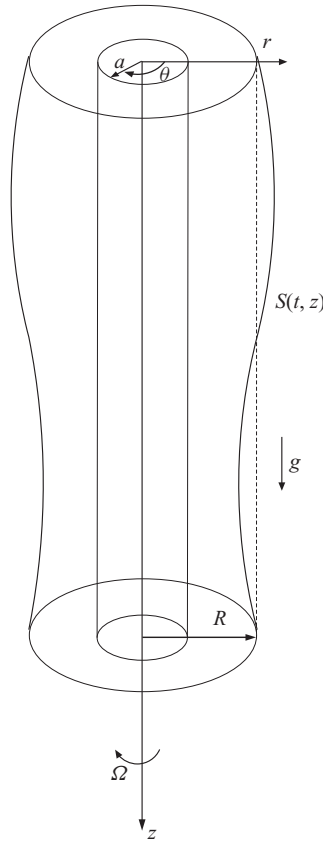


FIGURE 1. Sketch of the geometry of a film flow coating a fibre.

$$\partial_t w + u \partial_r w + \frac{v}{r} \partial_\theta w + w \partial_z w = g - \frac{\partial_z p}{\rho} + \frac{\mu}{\rho} \left[\partial_{rr} w + \frac{\partial_r w}{r} + \frac{\partial_{\theta\theta} w}{r^2} + \partial_{zz} w \right], \quad (2.4)$$

in which p is the pressure and \mathbf{u} is the velocity vector with u, v, w denoting the components in r, θ, z directions. In the rotating coordinates, two additional forces, i.e. the centrifugal $\rho \Omega^2 r \mathbf{e}_r$, and Coriolis force $2\rho \Omega \mathbf{e}_z \times \mathbf{u}$, have been added as external forces in the governing equations.

At the fibre wall, $r = a$, the velocity satisfies no-penetration and no-slip conditions

$$u = v = w = 0. \quad (2.5)$$

At the free surface, $r = S(\theta, z, t)$, the balance of the normal stress is

$$\mathbf{n} \cdot \mathbf{T} \cdot \mathbf{n} = 2\sigma H, \quad (2.6)$$

where the surface tension, σ , is constant. The balances of the shear stress are

$$\mathbf{t}_1 \cdot \mathbf{T} \cdot \mathbf{n} = 0, \quad (2.7)$$

$$\mathbf{t}_2 \cdot \mathbf{T} \cdot \mathbf{n} = 0, \quad (2.8)$$

where \mathbf{T} is the stress tensor

$$\mathbf{T} = \mu [\nabla \mathbf{u} + (\nabla \mathbf{u})^T], \quad (2.9)$$

t_1 , t_2 and n are the unit vectors tangential and normal to the interface

$$t_1 = \frac{(r^{-1}\partial_\theta S, 1, 0)}{\sqrt{1 + r^{-2}(\partial_\theta S)^2}}, \tag{2.10}$$

$$t_2 = \frac{(\partial_z S, 0, 1)}{\sqrt{1 + (\partial_z S)^2}}, \tag{2.11}$$

$$n = \frac{(1, -r^{-1}\partial_\theta S, -\partial_z S)}{\sqrt{1 + r^{-2}(\partial_\theta S)^2 + (\partial_z S)^2}}, \tag{2.12}$$

and $2H$ is the principal curvature of the surface

$$2H = -\frac{1}{N} \left\{ \frac{1}{S} + \frac{(\partial_\theta S)^2}{S^3} - \frac{\partial_{\theta\theta} S}{S^2} - \partial_{zz} S \right\} - \frac{1}{N^2} \left(\frac{\partial_\theta N \partial_\theta S}{S^2} + \partial_z S \partial_z N \right), \tag{2.13}$$

in which

$$N = \sqrt{1 + r^{-2}(\partial_\theta S)^2 + (\partial_z S)^2}. \tag{2.14}$$

The kinematic boundary condition on the free surface is

$$S_t + \frac{v}{r} \partial_\theta S + w \partial_z S = u, \tag{2.15}$$

or in conservative form

$$S_t + \frac{1}{S} \partial_\theta \int_a^S v \, dr + \frac{1}{S} \partial_z \int_a^S wr \, dr = 0. \tag{2.16}$$

2.1. Scalings

The non-dimensionalization is based on the viscous-gravity velocity, $V \equiv \rho g R^2 / \mu$, and the capillary length, $L = \sigma / \rho g R$. We assume that the radius of the fluid ring, R , is much smaller than the characteristic length L . The scalings are as follows:

$$\left. \begin{aligned} r = Rr^*, \quad z = Lz^*, \quad t = LV^{-1}t^*, \quad w = Vw^*, \quad u = \epsilon Vu^*, \quad v = \epsilon Vv^*, \\ p = \rho g L p^*, \quad S = RS^*, \quad a = Ra^*, \end{aligned} \right\} \tag{2.17}$$

where the aspect ratio parameter $\epsilon = R/L$ is a small number, and ‘*’ denotes non-dimensional variables. Here, we assumed that the azimuthal velocity is also small, i.e. $v \sim O(\epsilon)$.

For convenience, we drop the * decoration and the dimensionless Navier–Stokes equations are expressed as

$$\partial_r u + \frac{u}{r} + \frac{1}{r} \partial_\theta v + \partial_z w = 0, \tag{2.18}$$

$$\begin{aligned} \epsilon^4 Re \left(\partial_t u + u \partial_r u + \frac{v}{r} \partial_\theta u + w \partial_z u - \frac{v^2}{r} \right) \\ = -\partial_r p + \Omega_N r - 2\epsilon \alpha \Omega_N v + \epsilon^2 \left[\partial_{rr} u + \frac{\partial_r u}{r} + \frac{1}{r^2} \partial_{\theta\theta} u - \frac{u}{r^2} + \epsilon^2 \partial_{zz} u \right], \end{aligned} \tag{2.19}$$

$$\begin{aligned} \epsilon^4 Re \left(\partial_t v + u \partial_r v + \frac{v}{r} \partial_\theta v + w \partial_z v + \frac{uv}{r} \right) \\ = -\frac{1}{r} \partial_\theta p + 2\epsilon \alpha \Omega_N u + \epsilon^2 \left[\partial_{rr} v + \frac{\partial_r v}{r} + \frac{1}{r^2} \partial_{\theta\theta} v - \frac{v}{r^2} + \epsilon^2 \partial_{zz} v \right], \end{aligned} \tag{2.20}$$

$$\epsilon^2 Re \left(\partial_t w + u \partial_r w + \frac{v}{r} \partial_\theta w + w \partial_z w \right) = 1 - \partial_z p + \partial_{rr} w + \frac{\partial_r w}{r} + \frac{1}{r^2} \partial_{\theta\theta} w + \epsilon^2 \partial_{zz} w, \tag{2.21}$$

where the Reynolds number is defined as $Re = \rho VL/\mu$, and the parameters related to rotation are $\Omega_N = \Omega^2 R^2/gL$ and $\alpha = V/\Omega R$. This non-dimensionalization naturally results in $\epsilon = \rho g R^2/\sigma$, which is also referred to as the Bond number. The choice of small ϵ implies a small Bond number and surface-tension-dominated case. The full set of dimensionless parameters are $\epsilon, a, \Omega_N, \alpha$ and Re .

We choose the set of parameters used in the experiments by Kliakhandler *et al.* (2001), in which castor oil with density $\rho = 0.961 \times 10^3 \text{ kg m}^{-3}$, kinematic viscosity $\nu \equiv \mu/\rho = 4.44 \times 10^{-4} \text{ m}^2 \text{ s}^{-1}$, surface tension $\sigma = 3.1 \times 10^{-2} \text{ kg s}^{-2}$, is used for coating. The radius of the fluid ring in initial state, R , is approximately 1 mm. For this set of physical parameters, the dimensionless parameter ϵ is less than 0.3 and the Reynolds number $Re \sim 10^{-2}$. We fixed the radius of the initial surface to be approximately 1 mm and change the angular frequency of rotation $\Omega = 2\pi f$, in which f is the frequency measured in cycles per second or Hertz. As f changes in the range from 10 to 30 which is easily realized in experiments, $\Omega_N = 0.1223, 0.4890, 1.1003, \alpha = 0.3545, 0.1772, 0.1182$ for $f = 10, 20$ and 30 . When deriving the long-wave evolution equation, we assume the parameter Ω_N has order $O(1)$.

2.2. Linear stability

In the framework of normal mode analysis, the variables in the full Navier–Stokes equations are decomposed in the form of

$$[u, v, w, p, S] = [\bar{u}, \bar{v}, \bar{w}, \bar{p}, \bar{S}] + [\hat{u}, \hat{v}, \hat{w}, \hat{p}, \hat{S}] \exp[i(m\theta + kz - \omega t)], \tag{2.22}$$

in which ‘ $\bar{\cdot}$ ’, denotes the base state, ‘ $\hat{\cdot}$ ’, denotes the Fourier amplitudes of the disturbances, the integer m and the real number k denote the azimuthal and streamwise wavenumbers and ω denotes the frequency. The basic states of u, w and p are

$$\bar{u} = 0, \tag{2.23}$$

$$\bar{w} = \frac{1}{4}(a^2 - r^2) + \frac{1}{2} \ln \frac{r}{a}, \tag{2.24}$$

$$\bar{p} = 1 + \frac{1}{2} \Omega_N (r^2 - 1). \tag{2.25}$$

The governing equations for the disturbances are as follows:

$$D\hat{u} + \frac{\hat{u}}{r} + \frac{im}{r} \hat{v} + ik\hat{w} = 0, \tag{2.26}$$

$$\begin{aligned} \epsilon^4 Re(-i\omega \hat{u} + ik\bar{w}\hat{u}) \\ = -D\hat{p} - 2\epsilon \alpha \Omega_N \hat{v} + \epsilon^2 \left[D^2 \hat{u} + \frac{D\hat{u}}{r} - \left(\epsilon^2 k^2 + \frac{m^2 + 1}{r^2} \right) \hat{u} - \frac{2im\hat{v}}{r^2} \right], \end{aligned} \tag{2.27}$$

$$\begin{aligned} &\epsilon^4 \text{Re}(-i\omega \hat{v} + ik\bar{w}\hat{v}) \\ &= -\frac{im}{r}\hat{p} + 2\epsilon\alpha\Omega_N\hat{u} + \epsilon^2 \left[D^2\hat{v} + \frac{D\hat{v}}{r} - \left(\epsilon^2k^2 + \frac{m^2 + 1}{r^2} \right) \hat{v} + \frac{2im\hat{u}}{r^2} \right], \end{aligned} \tag{2.28}$$

$$\epsilon^2 \text{Re}(-i\omega\hat{w} + D\bar{w}\hat{u} + ik\bar{w}\hat{w}) = -ik\hat{p} + \left[D^2\hat{w} + \frac{D\hat{w}}{r} - \left(\epsilon^2k^2 + \frac{m^2}{r^2} \right) \hat{w} \right], \tag{2.29}$$

where $D = d/dr$.

At the fibre wall ($r = a$), the boundary conditions are

$$\hat{u} = \hat{v} = \hat{w} = 0. \tag{2.30}$$

At the perturbed surface, boundary conditions are projected to $r = 1$ and after linearising, we have

$$\hat{p} - 2\epsilon^2(D\hat{u} - ikD\bar{w}\hat{S}) = -(1 + \Omega_N\bar{S})\hat{S} + (m^2 + \epsilon^2k^2)\hat{S}, \tag{2.31}$$

$$D\hat{w} + D^2\bar{w}\hat{S} + i\epsilon^2k\hat{u} = 0, \tag{2.32}$$

$$rD\left(\frac{\hat{v}}{r}\right) + \frac{im}{r}\hat{u} = 0, \tag{2.33}$$

$$-i\omega\hat{S} + ik\bar{w}\hat{S} - \hat{u} = 0. \tag{2.34}$$

The fully linearized Navier–Stokes equations are solved by a Chebyshev collocation method.

Figure 2 shows the dispersion relations of the axisymmetric mode ($m = 0$) and the non-axisymmetric mode ($m = 1$). At $f = 0$, as shown in figure 2(a,d) for $a = 0.3$ and 0.8 , the axisymmetric mode is the most unstable. As $f = 10$ in figure 2(b,e), the non-axisymmetric mode with $m = 1$ becomes unstable in the long-wave range, but the maximum growth rate of $m = 1$ is less than that of $m = 0$. This indicates that the axisymmetric mode dominates the instability when the rotating speed is low. As f increases to 20, as shown in figure 2(c,f) the asymmetric mode $m = 1$ becomes the most unstable mode.

In figure 3, we compare the dispersion relation of axisymmetric disturbances predicted by the fully linearized Navier–Stokes equations with that of neglecting the Coriolis forces, i.e. setting α to be zero in (2.27) and (2.28). Figure 3 shows that the influence of the Coriolis forces on the stability is negligible when the rotating speed is low such that $\Omega_N \sim O(1)$. Therefore, in the following discussions, the Coriolis effect has been neglected.

We will examine the nonlinear evolution of the most unstable mode for both low and high frequencies of rotation. At low frequency of rotation, the most unstable is axisymmetric, i.e. $m = 0$. In this case, we derive an asymptotic model equation to describe the dynamics of the flow. In the fast rotation case, the results of the linear stability analysis have shown that the $m = 0$ is not the most unstable. We should note that there exists different transitional routes in the present system, which depends on the initial conditions. When the rotation is slow, if the initial condition takes the non-axisymmetric form and has no streamwise component (the $m = 0$ component), it can develop into a non-axisymmetric state because it is unstable. However, when the initial condition has a streamwise component, we observe that the final saturated state is axisymmetric, i.e. the non-axisymmetric mode is suppressed by the axisymmetric mode at small rotation number (see appendix B). When the rotation is fast, if we increase the rotation gradually

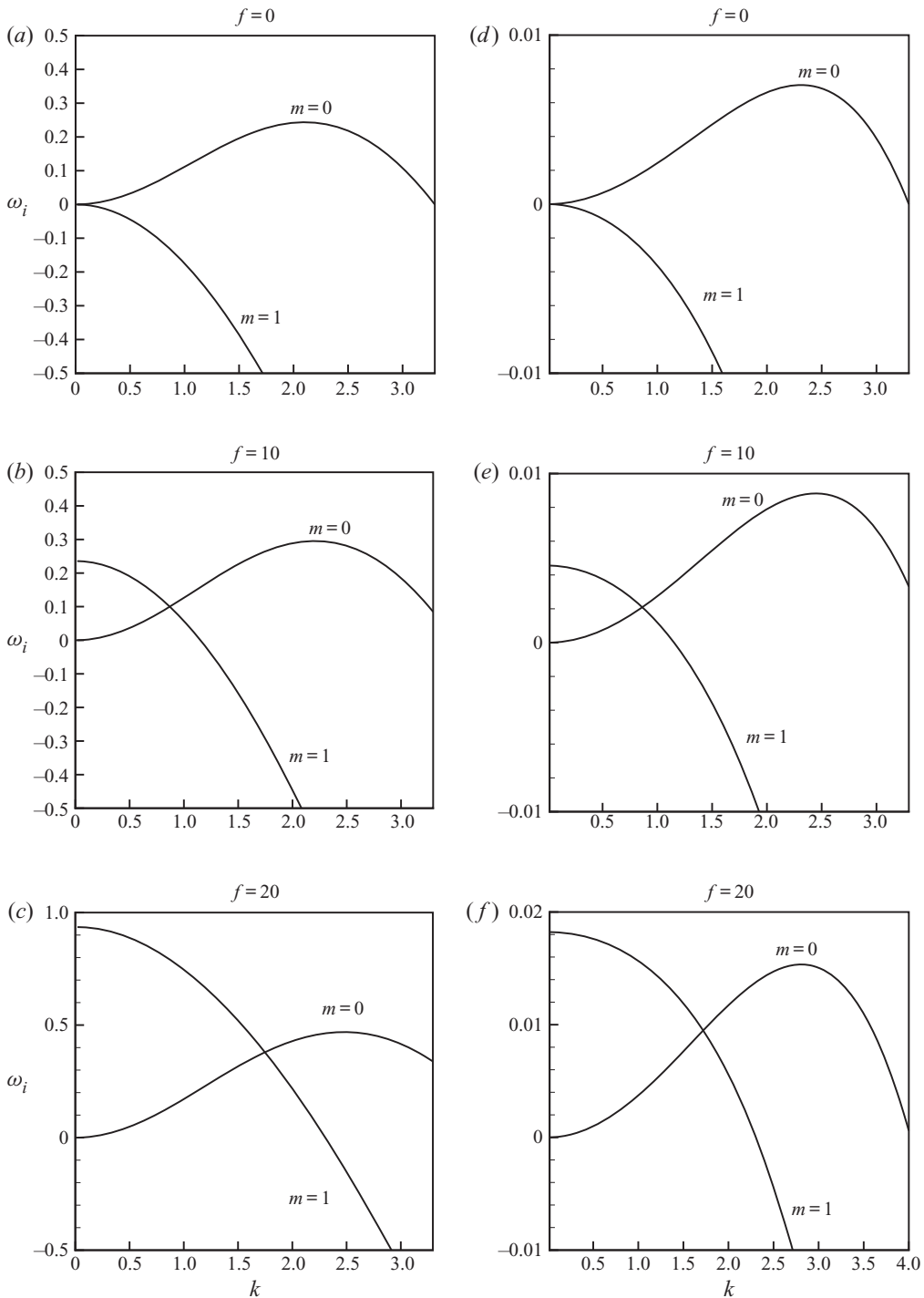


FIGURE 2. The curves of the dispersion relations predicted by the linearized Navier–Stokes equations (2.23)–(2.31) for (a) $a = 0.3, f = 0$; (b) $a = 0.3, f = 10$; (c) $a = 0.3, f = 20$; (d) $a = 0.8, f = 0$; (e) $a = 0.8, f = 10$; (f) $a = 0.8, f = 20$. Here, $f = 0$ corresponds the non-rotating case of $\Omega_N = 0$. At $f = 10$ and 20 , the parameters related to rotation, (Ω_N, α) , are $(0.1223, 0.3545)$ and $(0.4890, 0.1772)$, respectively. The parameter $\epsilon \approx 0.3$.

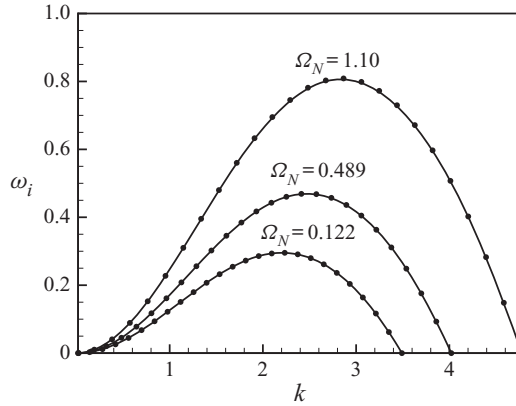


FIGURE 3. Comparison of the curves of the dispersion relations of axisymmetric modes with $m = 0$ predicted by the linearized Navier–Stokes equations (2.26)–(2.34) (solid lines) and the cases without Coriolis force (marked by solid circles). Other parameters are $a = 0.3$, $\epsilon \approx 0.3$. The parameter $\Omega_N = 0.122, 0.489, 1.10$ corresponds to $f = 10, 20, 30$, respectively.

and allow the axisymmetry mode to appear first, the non-axisymmetric mode ($m = 1$) will be bypassed, which has also been demonstrated by the simulation of a 3-D thin film model in appendix B. However, for a uniform film, if one suddenly rotates the cylinder at a high speed, the non-axisymmetric mode may appear first, which is confirmed by direct numerical simulation in appendices A and B. The axisymmetric state, however, might also be unstable to azimuthal disturbances, when the film is very thin. For example, Rietz *et al.* (2017) observed that axisymmetric ring waves lose instability to a rivulet structure. A similar transitional scenario has also been found in a liquid film flowing underneath an inclined plane (Charogiannis *et al.* 2018). It should be noted that the Rayleigh–Plateau mechanism is very weak and negligible in Rietz *et al.* (2017) due to the small thickness of film. In the present work, both the Rayleigh–Plateau mechanism and the Rayleigh–Taylor instability are important because the film is thick. It will be very challenging to investigate the rivulet instability in the present case because deriving a simple model equation is not possible. However, the present axisymmetric model can be applied to understand the nonlinear wave dynamics on the crests of rivulets formed on the fibre, e.g. the interaction between different waves leading to an oscillating state.

2.3. A long-wave model

The linear stability analysis shows that the Coriolis effect is negligible at small rotation frequency, $\Omega_N = O(1)$. The axisymmetric unstable mode dominates the primary instability when the rotating frequency is low $f \leq 10$ and surface tension effect is dominant (small ϵ). Assuming $\epsilon^2 \ll 1$, $Re \sim O(1)$ and slow rotation, we can neglect the inertial terms and the Coriolis force.

Under the assumption of axisymmetry, the leading-order Navier–Stokes equation is given by

$$0 = -\partial_r p + \Omega_N r, \tag{2.35}$$

$$\partial_{rr} w + \frac{\partial_r w}{r} = \partial_z p - 1. \tag{2.36}$$

At the fibre wall $r = a$,

$$w = 0. \tag{2.37}$$

The leading-order tangential and normal stress balances at the surface ($r = S$) are

$$\partial_r w = 0, \tag{2.38}$$

$$p = \frac{1}{S} - \epsilon^2 \partial_{zz} S. \tag{2.39}$$

It is notable that the term, $\epsilon^2 S_{zz}$, which involves the highest derivative of S is included in (2.39). In a linear analysis, the inclusion of this term is vital to give the correct cutoff wavenumber. Conventionally, this term is kept in long-wave theories of the problem with a cylindrical free surface, such as jets, threads and liquid bridges (Eggers & Dupont 1994; Craster & Matar 2006). An understandable explanation for the inclusion of this term is that the streamwise curvature is sufficiently large in some regions at the interface such as the steep front edge of a solitary hump. So, the term which contains the highest derivative of S is sufficiently large and cannot be neglected even though it is multiplied by ϵ^2 . For more justification of the inclusion of this term, we refer the reader to Craster & Matar (2006). An alternative choice is to keep the full curvature in the equation of the balance of the normal stresses in other related topics, for example, free-surface flows with large slopes (Snoeijer 2006) and rim or coating flows (Lopes, Thiele & Hazel 2018).

From (2.35) and (2.36), we obtain the pressure

$$p = \frac{1}{S} - \epsilon^2 \partial_{zz} S + \frac{1}{2} \Omega_N (r^2 - S^2), \tag{2.40}$$

and the velocity $w(r, z, t)$

$$w = (1 - \partial_z p) \left[\frac{1}{4} (a^2 - r^2) + \frac{1}{2} S^2 \ln \frac{r}{a} \right]. \tag{2.41}$$

Substituting w into the kinematic boundary condition yields an evolution equation for $S(z, t)$ given by

$$\partial_t S = -\frac{1}{16S} \partial_z \left\{ \left(1 + \frac{\partial_z S}{S^2} + \Omega_N S \partial_z S + \epsilon^2 \partial_{zzz} S \right) \left[4S^4 \log \frac{S}{a} + (3S^2 - a^2)(a^2 - S^2) \right] \right\}. \tag{2.42}$$

Equation (2.42) is identical to Craster & Matar (2006) when the rotation is turned off.

2.4. Thin film limit

For the case in which the film is thin relative to the fibre, i.e. $S(z, t) = a + h(z, t)$, where the film thickness $h \ll a$, expanding equation (2.42) for small h results in the evolution equation for the thin film

$$\left(1 + \frac{h}{a} \right) \partial_t h + \frac{1}{3} \frac{\partial}{\partial z} \times \left\{ h^3 \left(1 + \frac{h}{a} \right) \left[1 + \frac{\partial_z h}{a^2 (1 + h/a)^2} + \Omega_N a (1 + h/a) \partial_z h + \epsilon^2 \partial_{zzz} h \right] \right\} = 0. \tag{2.43}$$

For very thin fluid films, $a \rightarrow 1$ and $1 + h/a \rightarrow 1$, the evolution equation can be further simplified as

$$\partial_t h + \frac{\partial}{\partial z} \left\{ \frac{h^3}{3} \left[1 + (1 + \Omega_N) \partial_z h + \epsilon^2 \partial_{zzz} h \right] \right\} = 0. \tag{2.44}$$

At $\Omega_N = 0$, (2.44) is reduced to the evolution equation of thin film by some authors (Frenkel 1992; Kalliadasis & Chang 1994). The roles of capillary forces and rotation on the stability of the film are manifested in (2.44). The terms $\partial_z h$, $\Omega_N \partial_z h$, $\epsilon^2 \partial_{zzz} h$ denote the contributions of azimuthal curvature, the rotation and the streamwise curvature, respectively. It is well known that the azimuthal curvature and the streamwise curvature are destabilizing and stabilizing, respectively (Kliakhandler *et al.* 2001; Craster & Matar 2006). From (2.44) for the thin film limit, it can be seen that the rotation is destabilizing the interface through the azimuthal curvature.

3. Linear stability analysis of the long-wave model

3.1. Dispersion relations

Let us now consider the linear stability of the problem. A small periodic disturbance in the streamwise direction is imposed on the film such that the film thickness can be decomposed into a base state component \bar{S} , and a small disturbance of normal mode with amplitude \hat{S} ,

$$S = \bar{S} + \hat{S}e^{i(kz - \omega t)}, \quad (3.1)$$

in which ω is the complex frequency and k is the wavenumber, and $\bar{S} = 1$.

Substituting (3.1) into (2.42) yields the dispersion relation

$$-i\omega + \left\{ \frac{1}{16}k^2(k^2\epsilon^2 - (1 + \Omega_N)) \left(4 \ln \frac{1}{a} - a^4 + 4a^2 - 3 \right) + \frac{ik}{2}(a^2 - 1 - 2 \ln a) \right\} = 0. \quad (3.2)$$

At $\Omega_N = 0$, this dispersion relation is identical to that of Craster & Matar (2006) for a coating flow down a fibre. In the thin film limit as $a \rightarrow 1$, the dispersion relation corresponding to (2.44) tends to

$$-i\omega \sim \frac{1}{3}k^2[(1 + \Omega_N) - k^2\epsilon^2](1 - a)^3 - ik(1 - a)^2. \quad (3.3)$$

We use ω_r and ω_i to denote the real part and imaginary part of ω . Here, ω_i and ω_r correspond to its growth or decay rate and the frequency of the disturbance. The phase speed of the disturbance is defined as $c = k^{-1}\omega_r$. From (3.2), the phase speed

$$c = \frac{1}{2}(a^2 - 1 - 2 \ln a), \quad (3.4)$$

is positive and independent of the wavenumber k and the rotation parameter Ω_N . This means all disturbances with different wavenumbers propagate downstream at a same speed.

Craster & Matar (2006) have tested the validity of their model by comparing the results of the dispersion relation predicted by the long-wave model and the linear stability characteristics of the Stokes flow equations. The result showed that the model equation provides a reasonably good approximation of the full Navier–Stokes equations. In the present paper, we will test the validity of the model (2.42) with the presence of rotation. The details of the stability analysis of the full Navier–Stokes equations are presented in § 2.2. In order to know quantitatively the effect of rotation, in figure 4 we plot the curves of the dispersion relations (3.2) of the long-wave model and those via fully linear stability analysis.

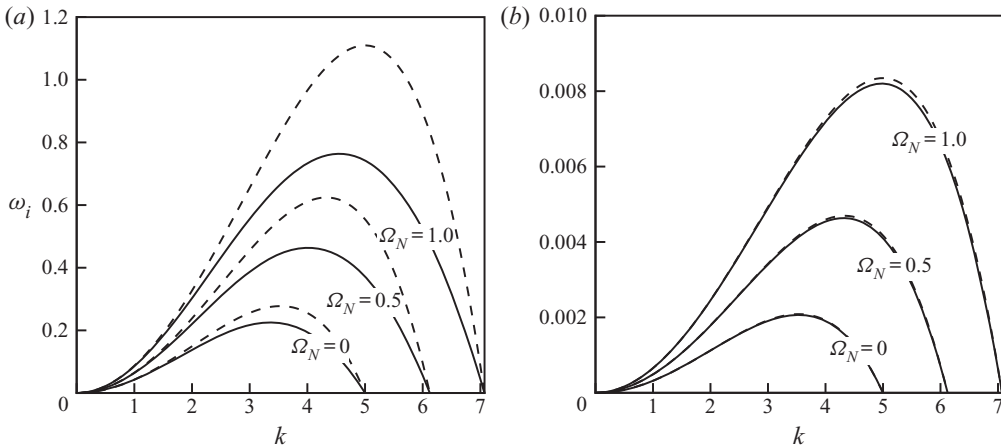


FIGURE 4. Comparisons of the real growth rate of the axisymmetric mode $m = 0$ versus the wavenumber in the range of $0 < k < k_c$ for various Ω_N between the stability analysis of the Navier–Stokes equations (solid lines) and the long-wave model (dashed lines). Other parameters are $\epsilon = 0.2$, (a) $a = 0.5$, (b) $a = 0.9$.

We compared the dispersion relations for both models for two typical cases, thick film with $a = 0.5$ and thin film with $a = 0.9$. Inspection of the dispersion curves indicates that the prediction of the long-wave model is in reasonable agreement with that predicted by the Navier–Stokes equations for various Ω_N . For a fixed k , both models predict that the growth rate ω_i increases with the increase of Ω_N . In figure 4(a), we observed that for thick film the time growth rate predicted by the long-wave model is obviously higher than that predicted by the linear stability analysis. However, in figure 4(b), the agreement between both models is excellent for the case of thin film.

3.2. Absolute and convective instabilities

For a general hydrodynamics stability problem, the wavenumber and frequency satisfy a dispersion relation in the form of

$$D(k, \omega) = 0. \tag{3.5}$$

In this subsection, we carry out a spatio-temporal stability analysis and both the wavenumber k and the frequency ω are complex numbers.

The stability properties of the perturbations are determined by the long-time behaviour of an impulsive response to a localized excitation. The solution of the impulsive response can be expressed in the form of

$$G(z, t) = \frac{1}{2\pi} \int_A \int_F \frac{e^{i(kz - \omega t)}}{D(k, \omega)} d\omega dk, \tag{3.6}$$

where the Bromwich contour F in the ω -plane is a horizontal line lying above all the singularities to satisfy causality, and the integration path A lies inside the analyticity band around the k -axis.

The nature of CI and AI can be identified by examining the long-time behaviour of the wavenumber k_0 along the ray z/t at a fixed spatial location. This complex k_0 has, by

definition, a zero group velocity

$$\frac{\partial \omega}{\partial k}(k_0) = 0, \tag{3.7}$$

and $\omega_0 = \omega(k_0)$ is called the absolute frequency. If $\text{Im}(\omega_0) > 0/\text{Im}(\omega_0) < 0$, the flow is said to be absolutely/convectively unstable. It should be noted that the saddle point k_0 must be identified by the Briggs–Bers collision criterion (Briggs 1964; Bers 1975), i.e. the saddle point must be a pinch point produced by the collision of two distinct spatial branches of solutions coming from the upper and lower half- k -planes. In the pinching process, when ω moves from above along the vertical line down to ω_0 , the two spatial branches $k_1(\omega)$ and $k_2(\omega)$ originate in this movement on opposite sides of the real k -axis and collide at $k = k_0$ and $\omega = \omega_0$. For more details on the topics related to AI–CI problems, we refer the reader to a good review article by Huerre & Monkewitz (1990). The most relevant work to the present problem is the study on the AI–CI characteristics of an exterior coating film down a vertical fibre (Duprat *et al.* 2007). Very recently, an experimental study by Sadeghpour *et al.* (2019) also showed that the water–vapour transfer rate in the coating flow is dependent on the AI–CI characteristics. For example, when the flow is absolutely unstable, the water–vapour transfer rate is generally promoted by increasing the liquid flow rate. However, in the convectively unstable situation, the water–vapour transfer rate does not increase with the liquid flow rate due to the occurrence of irregular beads.

From the dispersion relation, (3.2), the complex frequency ω can be expressed as a polynomial of k :

$$\omega = \frac{i}{16}k^2[(1 + \Omega_N) - \epsilon^2k^2]f_1 + kf_2, \tag{3.8}$$

in which

$$f_1 = 4 \ln \frac{1}{a} - a^4 + 4a^2 - 3, \tag{3.9}$$

$$f_2 = \frac{1}{2}(a^2 - 1 - 2 \ln a). \tag{3.10}$$

Through the transformation $k = \alpha \tilde{k}$, $\beta = (1 + \Omega_N)(\alpha\epsilon)^{-2}$, $\tilde{\omega} = \omega(\alpha f_2)^{-1}$, where $\alpha = [(16f_2)/(3f_1\epsilon^2)]^{1/3}$, the dispersion relation reduces to a standard form as

$$\tilde{\omega} = \tilde{k} + \frac{i\tilde{k}^2}{3}(\beta - \tilde{k}^2). \tag{3.11}$$

A straightforward analysis based on (3.11) then shows that the instability becomes absolute when $\beta > \beta_c = [(9/4)(-17 + 7\sqrt{7})]^{1/3} \approx 1.5$ (Duprat *et al.* 2007). Therefore, applying $\beta = (1 + \Omega_N)(\alpha\epsilon)^{-2}$ to the condition $\beta > \beta_c$ yields the following implicit condition for absolute instability:

$$(1 + \Omega_N) \left(\frac{3f_1}{16\epsilon f_2} \right)^{2/3} > \beta_c. \tag{3.12}$$

In figure 5(a,b), we present the AI–CI boundaries for various Ω_N in the ϵ – a plane and for various a in the ϵ – Ω_N plane, respectively. The range of parameter a is (0, 1). The model is valid for small ϵ , however, when presenting the results we extend the range of ϵ to 0.5. As shown in figure 5(a), for each curve with the decrease of a or ϵ the flow regime can switch from convective instability to absolute instability. With the increase of Ω_N , the absolutely

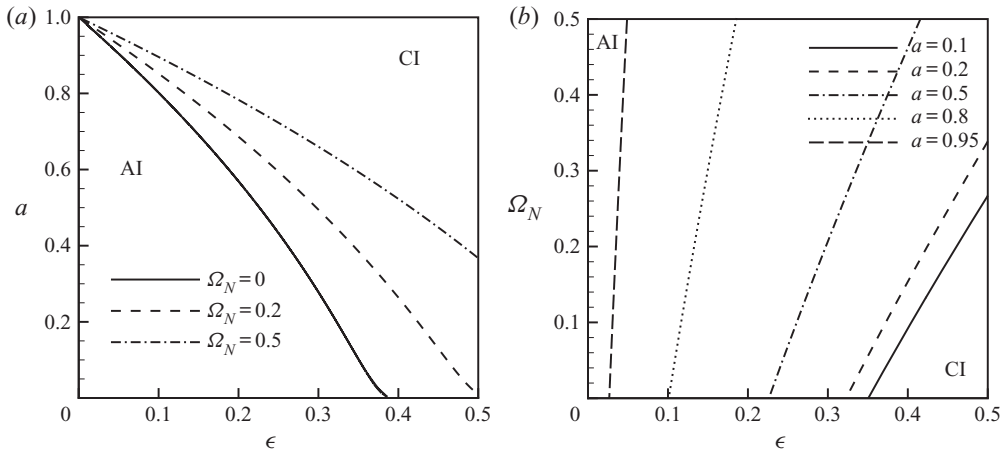


FIGURE 5. The boundaries between CI and AI, (a) in the ϵ - a plane for various Ω_N , (b) in the ϵ - Ω_N plane for various a .

unstable regime extends in the ϵ - a plane. In figure 5(a), as $\Omega_N = 0$ the convective regime occupies a large portion of area in the ϵ - a plane. With the increase of Ω_N , some CI regimes become absolutely unstable and the boundary extends counterclockwise in the ϵ - a plane. In figure 5(b), it is shown that for each value of a with the increase of Ω_N the flow switches from the CI to the AI regime. The results of figure 5 indicate that the increase of rotation promotes the absolute instability.

4. Nonlinear evolutions

In this section, we will study the nonlinear evolution from the initial state seeded with small disturbances. Equation (2.42) subject to periodic boundary conditions was solved numerically using a Fourier spectral method. The solution of $S(z, t)$ is expanded by the Fourier series

$$S(z, t) = \sum_{-N/2}^{N/2} \hat{s}_n(t) \exp \left[i \frac{2\pi n z}{l} \right], \tag{4.1}$$

in which N is the number of Fourier modes, $\hat{s}_n(t)$ is the time-dependent coefficient and l is the computational length. A Fourier collocation is used to provide the discretization in space for periodic problem. We employed an implicit Gear's method for stiff problems for the time stepping and the relative error is 10^{-6} at each time step (Ding & Willis 2019).

4.1. AI-CI instability

In this subsection, we performed numerical simulations on the nonlinear evolution of (2.42) to examine the effect of rotation on the transition from CI to AI regimes. We choose the set of parameters of $a = 0.3$ and $\epsilon = 0.4$ which lies in the CI regime for $\Omega_N = 0$ and in the AI regime for $\Omega_N = 0.5$. The initial condition is seeded with $S(z, 0) = 0.1 \exp[-(z - 20)^2/2]$ and the length of computational domain $l = 100$.

In figure 6, we present the spatio-temporal diagram for various Ω_N , which may be helpful for us to understand the effect of rotation on the AI-CI characteristics. For $\Omega_N = 0$, the flow is linearly convectively unstable. In figure 6(a) it is obvious that the disturbance

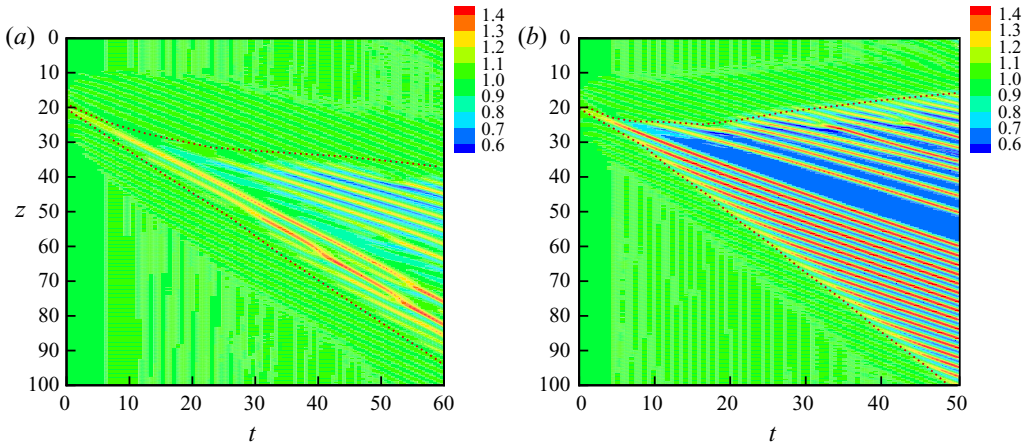


FIGURE 6. Spatial-temporal diagram for $a = 0.3$, $\epsilon = 0.4$. The values of $S(z, t)$ are marked by different colours. (a) $\Omega_N = 0$; (b) $\Omega_N = 0.5$.

propagates downstream and decays at $z = 20$. As Ω_N increases to 0.5, as shown in figure 5, the flow is absolutely unstable as the point of $(0.4, 0.3)$ in the ϵ - a plane is below the AI-CI boundary of $\Omega_N = 0.5$. In figure 6(b), as $\Omega_N = 0.5$, the flow becomes absolutely unstable as the disturbance is amplified both downstream and upstream.

4.2. Transient simulations in long domains

In order to know the properties of the solutions which are naturally selected, we performed numerical simulations in long domains subject to a pseudo-random initial condition. Two typical sets of parameters of a and ϵ are chosen. Kliakhandler *et al.* (2001) and Craster & Matar (2006) have performed simulations on the nonlinear evolution for three regimes in Kliakhandler *et al.* (2001) and all of them are in the absolute instability regime. The first set of parameters, $a = 0.255$ and $\epsilon = 0.292$ chosen in this paper, which falls in the absolute instability regime, is identical to that used by Kliakhandler *et al.* (2001) and Craster & Matar (2006). The second set of parameters, $a = 0.55$ and $\epsilon = 0.3$, however, is picked from the convectively unstable regime when $\Omega_N = 0$, which becomes absolutely unstable when $\Omega_N > 0.2$.

The system becomes saturated after long-time evolution. In figure 7, we present the results of the first set of parameters, which is in the absolutely unstable regime. In figure 7(a-d), similar-sized large droplets are moving as a bound state. The heights of these droplets are very close but the gaps between them can vary. The increase of Ω_N leads to the formation of more pronounced and closely spaced beads with smaller sizes. Moreover, the gaps between different beads become flatter and thinner.

Figure 8 shows the film profiles for different values of Ω_N , which demonstrates that the rotation has a significant influence on the flow pattern. In these figures, the height of the beads increases with the increase of Ω_N . Comparing with figure 8(a,c), in which Ω_N increases from $\Omega_N = 0$ to $\Omega_N = 0.5$, the height of the beads in figure 8(c) is obviously larger than that in figure 8(a). However, the large droplet numbers are reduced from six to two. Hence, the gap between the large drops in figure 8(c) is much longer than that in figure 8(a). This long film between the two large droplets in figure 8(c) is unstable and breaks into several tiny beads. The large droplet, however, will catch up with and consume

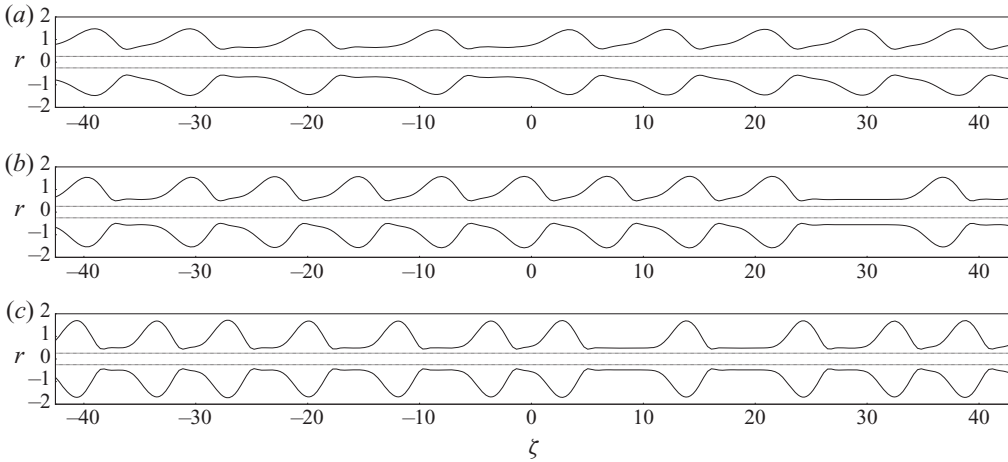


FIGURE 7. The profiles of the interface via transient numerical simulations for various Ω_N . Other parameters are $a = 0.2551$, $\epsilon = 0.2915$. The instant time is $t = 100$. The coordinate $\zeta = z/\epsilon$. Here, $\Omega_N = 0, 0.2, 0.5$ for (a), (b) and (c), respectively.

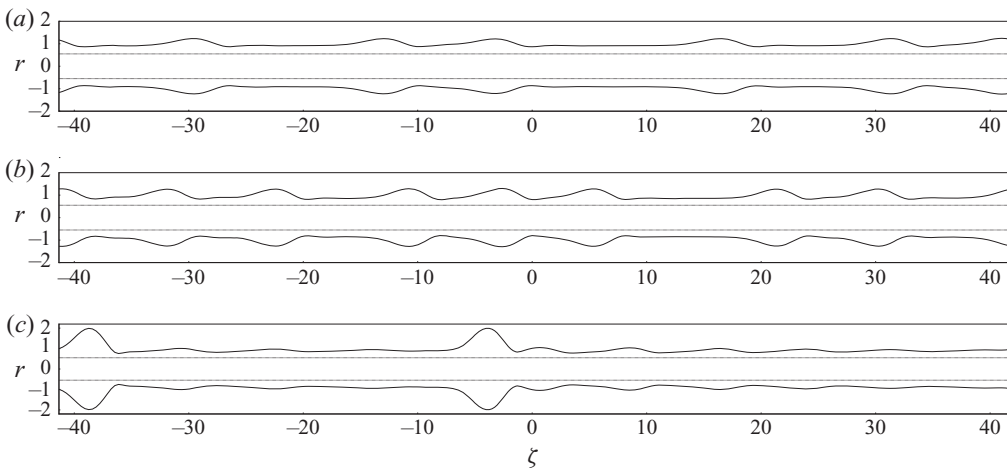


FIGURE 8. The profiles of the interface via transient numerical simulations for various Ω_N . Other parameters $a = 0.55$, $\epsilon = 0.3$. The instant time is $t = 500$. The coordinate $\zeta = z/\epsilon$. Here, $\Omega_N = 0, 0.2, 0.5$ for (a), (b), (c), respectively.

these small beads ahead and leave behind a flat film where small beads will regenerate again.

5. Travelling-wave solutions and their stabilities

5.1. Travelling-wave solutions

Experiments have shown different types of steadily propagating solutions in the form of highly organized droplets or bead-like solutions separated by long space (Kliakhandler *et al.* 2001). In this subsection, we will examine how rotation influences the characteristics of these steady travelling-wave solutions.

We solve the governing equations by moving to a travelling-wave coordinate. In the moving system, it is convenient to define

$$\tau = t, \quad (5.1)$$

$$\xi = z - ct, \quad (5.2)$$

where c is the wave speed of the moving coordinate. The derivatives with respect to t and z can be expressed as

$$\partial_t = \partial_\tau - c\partial_\xi, \quad (5.3)$$

$$\partial_z = \partial_\xi. \quad (5.4)$$

For a travelling-wave solution, the time derivation of S with respect to τ is zero, and the profile of the interface has the form of $S = S(\xi)$. The nonlinear equation (2.42) becomes

$$-c\partial_\xi S^2 + 2\partial_\xi Q(S) = 0, \quad (5.5)$$

where

$$Q(S) = \frac{1}{16} \left(1 + \frac{\partial_\xi S}{S^2} + \Omega_N S \partial_\xi S + \epsilon^2 \partial_{\xi\xi\xi} S \right) \left[4S^4 \log \frac{S}{a} + (3S^2 - a^2)(a^2 - S^2) \right]. \quad (5.6)$$

Integrating equation (5.5) once, we have

$$-cS^2 + 2Q(S) = q, \quad (5.7)$$

where q is an integral constant. Equation (5.7) subject to periodic boundary conditions will be solved in the region of $-l/2 < \xi \leq l/2$, where the length of the computational domain, l , is the wavelength of the travelling-wave solution. To fix c , we impose the mass conservative condition

$$\int_{-l/2}^{l/2} (S^2(\xi) - a^2) d\xi = l(1 - a^2). \quad (5.8)$$

To break the translational symmetry, one can enforce the real (or imaginary) part of the first Fourier mode to zero such that q can be determined. A code for Newton iteration based on Ding & Willis (2019) was developed to solve the present problem. The solution can be tracked from the Hopf bifurcation point ($\omega_i = 0$) with branch continuation.

Typical profiles of the travelling-wave solutions are shown in figure 9. As shown in figure 9, the droplet height is increased by the axial rotation. In Craster & Matar (2006) and Ding & Willis (2019), an observation is that higher droplets are moving faster than lower droplets. However, in the present study, it is found that this conclusion holds only if the axial rotation is slow (see figure 10a, in which the wave speed c increases with Ω_N). When the rotation becomes fast ($\Omega_N > 0.5$), we observe that large droplets can move slower than small droplets (see figure 10b), which is contrary to the conclusions of Craster & Matar (2006) and Ding & Willis (2019).

To account for the physical mechanism of the abnormal phenomenon, we plot the flow field in figure 11 in the moving frame. It indicates that the reversal flow in the wave hump becomes stronger as Ω_N increases. This reversal flow can significantly increase the viscous dissipation effect. In their work, Ruyer-Quil *et al.* (2008) derived a weighted residual

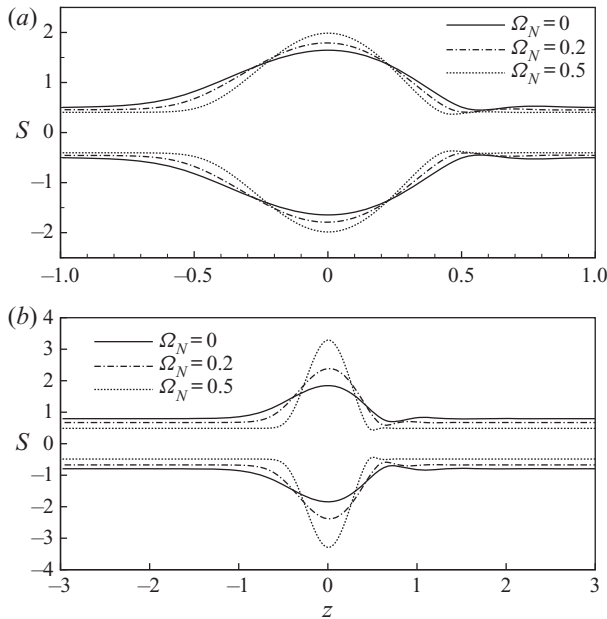


FIGURE 9. Interface profile for the travelling-wave solution for various Ω_N . Other parameters are $\epsilon = 0.2$ and $a = 0.25$. (a) $l = 2$; (b) $l = 6$.

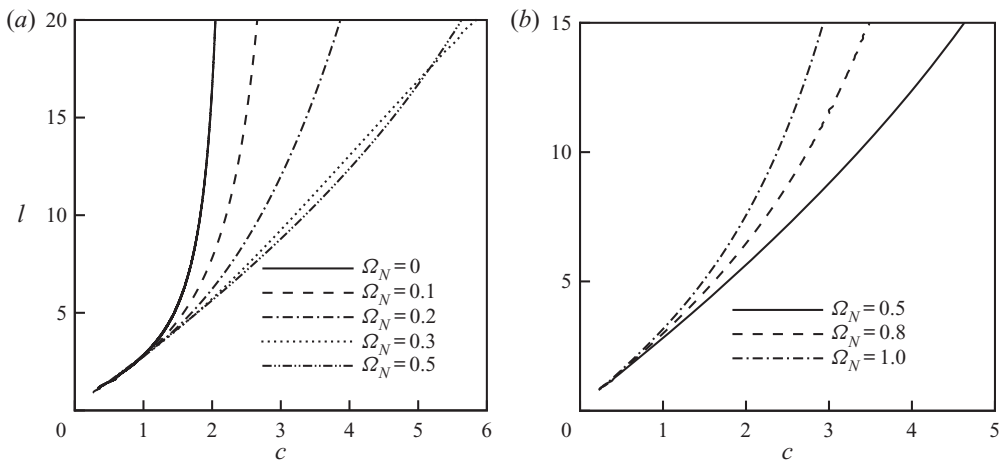


FIGURE 10. Travelling-wave solution for one-hump solutions: spacings l and propagating speeds c for various Ω_N at $\epsilon = 0.2$ and $a = 0.25$.

model, which considered the streamwise dissipation effect, and they found that the wave speed of the travelling-wave solution in flow regime ‘c’ is lower than Craster & Matar (2006). As also discussed by Ding & Willis (2019) that viscous dissipation effect can slow the droplet motion, it is suggestive that the motion of large droplets is retarded by this strong reversal flow in the hump.

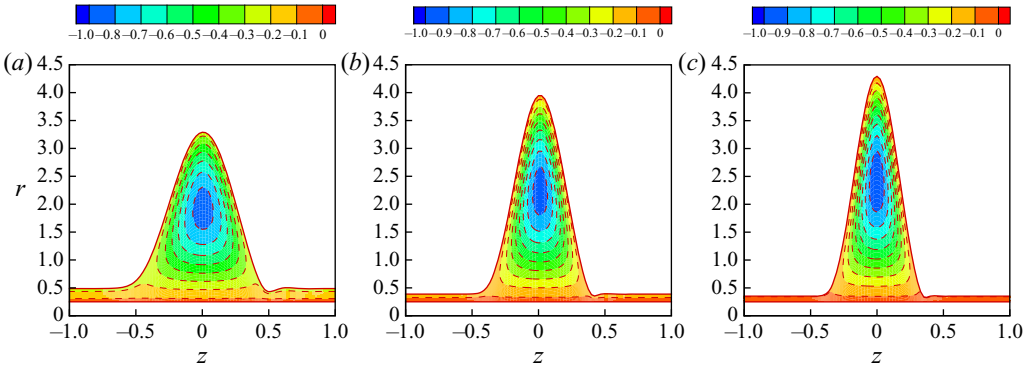


FIGURE 11. The flow field in the moving frame at $\Omega_N = 0.5, 0.8, 1$ for (a), (b) and (c), respectively.

5.2. Stability of the travelling-wave solution

Numerical simulations of the present problem showed that not all the travelling waves can be obtained through the evolution of an initial condition. It is natural to examine whether the travelling-wave solutions with different wavelengths are stable.

We performed a linear stability analysis on the travelling-wave solutions in the moving frame at the wave speed c . The profile of the interface is the travelling-wave solutions perturbed by an infinitesimal disturbance

$$S(\xi, \tau) = \bar{S}(\xi) + S'(\xi, \tau), \tag{5.9}$$

in which $S'(\xi, \tau) = \hat{S}(\xi)e^{-i\omega\tau}$.

The linearized evolution equation is written as

$$\bar{S}\partial_\tau S' - c\partial_\xi(\bar{S}S') + \partial_\xi\{(1 - \partial_\xi\bar{p})\mathcal{F}_S S' - \mathcal{F}\partial_\xi p'\} = 0, \tag{5.10}$$

in which

$$\partial_\xi\bar{p} = -\frac{\bar{S}_\xi}{\bar{S}^2} - \epsilon^2\partial_{\xi\xi\xi}\bar{S} - \Omega_N\bar{S}\partial_\xi\bar{S}, \tag{5.11}$$

$$\partial_\xi p' = -\frac{\partial_\xi S'}{\bar{S}^2} + 2\partial_\xi\bar{S}\frac{S'}{\bar{S}^3} - \epsilon^2\partial_{\xi\xi\xi}S' - \Omega_N(\bar{S}\partial_\xi S' + \partial_\xi\bar{S}S'), \tag{5.12}$$

$$\mathcal{F}_S = \bar{S}^3 \ln \frac{\bar{S}}{a} + \frac{\bar{S}(a^2 - \bar{S}^2)}{2}, \tag{5.13}$$

$$\mathcal{F} = \frac{\bar{S}^4}{4} \ln \frac{\bar{S}}{a} + \frac{(3\bar{S}^2 - a^2)(a^2 - \bar{S}^2)}{16}. \tag{5.14}$$

The curves of the leading eigenvalue of the travelling-wave solutions versus the wavelength are shown in figure 12. For $\Omega_N = 0$, there exists a critical wavelength $l_c \approx 3.5$ beyond which the travelling-wave solutions are unstable. As $l > l_c$, a conjugate complex pair of eigenvalues are found. In figure 12(a), the curves of the growth rate consists of several segments, indicating that mode switching occurs as l increases. This is also reflected by the non-continuous curves of temporal frequency ω_r as shown in figure 12(b). As shown in figure 12(a), with the increase of Ω_N the critical wavelength

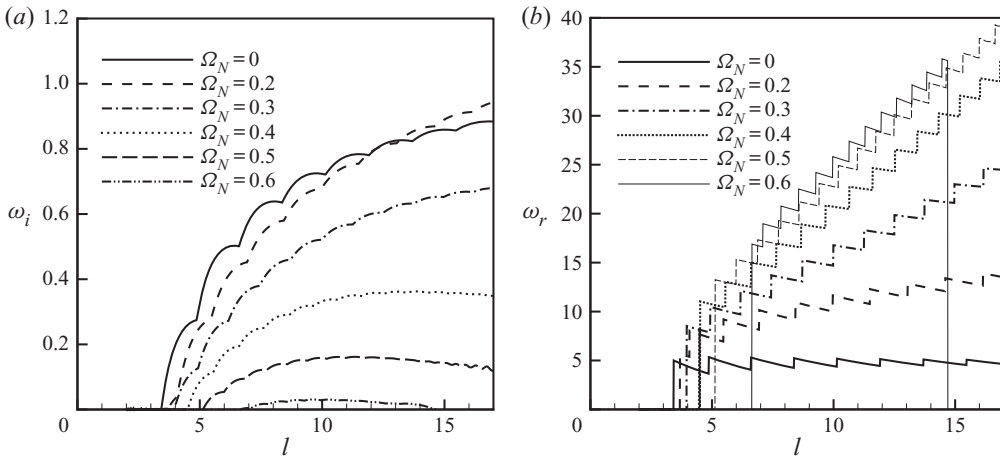


FIGURE 12. The curves of the leading eigenvalue for the travelling-wave solutions versus the wave length l . (a) The time growth rate ω_i , (b) the frequency ω_r . Other parameters are $\epsilon = 0.2$ and $a = 0.25$.

l_c increases. As Ω_N increases from 0 to 0.2, the growth rate decreases as $l < 12$ and increases as $l > 12$. As Ω_N increases from 0.2 to 0.6, the effect of rotation is stabilizing. In figure 12(a), for $\Omega_N = 0.6$ the unstable region is confined in a limited band of l . When Ω_N increases further, the travelling-wave solutions become completely stable. In figure 12(b), the frequency of the most unstable mode increases with the increase of Ω_N . The results in figure 12 showed that the effect of rotation on the travelling-wave solution is adverse to the linear stability of the trivial base state $\bar{S} = 1$ in which the rotation is destabilizing.

It is interesting to examine the structures of the most unstable mode of different segments in figure 12(a). In figure 13, the profiles of the most unstable mode are plotted for two typical sets of parameters. The structures of the disturbances are similar in these two figures. The disturbance consists of a series of ripples occupying the whole spatial domain. The disturbed surface is in the form of a large bead accompanied by a series of smaller beads. We also examine the structures of the most unstable mode for various parameters of l and Ω_N . The results of the linear stability analysis indicate that the structures of different segments are similar. The slight difference is that the numbers of small ripples may increase with l . It is obvious that the profiles in figure 13 provide initial states involving the interaction between a large bead and several smaller ones.

In the experiments by Kliakhandler *et al.* (2001), the flow regime ‘c’ presents dynamic behaviours different from the steady travelling waves, in which a complicated interaction between a large droplet and several small droplets causes an oscillatory flow. It is interesting to investigate how the rotation influences the dynamics of the oscillatory flow, i.e. flow regime ‘c’. To answer this question, we perform numerical simulations on the evolution initiated by a travelling-wave solution superposed of the most unstable mode. Before we study the nonlinear evolution by numerical simulations, it is helpful to discuss the nature of the stability of travelling-wave solutions. We classify the stability of travelling-wave solutions as being either convectively unstable or absolutely unstable. If the travelling-wave solutions are convectively unstable, they can tolerate localized disturbances and the flow ultimately evolves into a state in which the travelling waves interact with small ripples. If the travelling-wave solutions are absolutely unstable, these

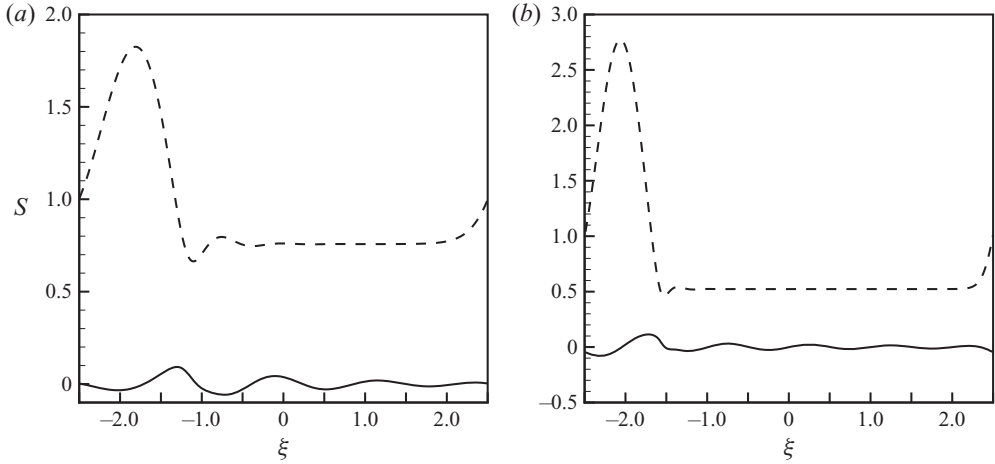


FIGURE 13. The profile of the leading unstable mode with $L = 5$. (a) $\Omega_N = 0$; (b) $\Omega_N = 0.4$. The dashed line denotes the basic state. Other parameters are $\epsilon = 0.2$ and $a = 0.25$.

solutions can be destroyed by localized disturbances and evolve into a new state after a long time of evolution. As discussed in figure 13, the eigenvalues corresponding to the most unstable modes are in the form of a pair of conjugated complex numbers. This means the most unstable mode is convectively unstable and can escape the travelling wave downstream or upstream. For related discussion on the stability of a two-dimensional pulse on electrified falling films, see Blyth *et al.* (2018).

In figure 14, the space–time diagrams of a long-time evolution are plotted for several typical cases. In figure 14(a) for $l = 4$ and $\Omega_N = 0$ in which the travelling-wave solution is unstable as shown in figure 12, the oscillatory behaviour of the height of the large droplets is obvious. In this space–time diagram, it is observed that the oscillation is both temporally and spatially periodic. In figure 14(b) for $l = 4$ and $\Omega_N = 0.4$, there is no oscillation in the space–time diagram, indicating the system is a steady travelling wave. In figure 14(c,d), the space–time diagrams are plotted for two typical cases with $l = 7$ in which the travelling-wave solutions are unstable. The characteristics of the structures in figure 14(a,c,d) are qualitatively similar. In these figures, smaller ripples arrange periodically in the z – t plane, and the loci of the large droplets oscillate periodically. The flow can be considered as an oscillatory travelling wave, which conforms to the fact that the travelling-wave solutions are convectively unstable. The numerical simulations suggest that the time-periodic state is a relative periodic orbit (RPO), which has been reported by Ding & Willis (2019) in a non-rotating system. However, it is unclear how the rotation affects the mean speed and the period of the RPO. We will proceed to § 5.3 to answer this question.

5.3. Exact RPOs

To find the exact RPOs of the present problem, we search for the recurrent solutions in the system

$$S(z, t) = S(z + s, t + T), \quad (5.15)$$

where s is the spatial shift along the axis of the fibre and T is the time period. Each RPO has its own particular period T , while a travelling wave has arbitrary period T . Given an

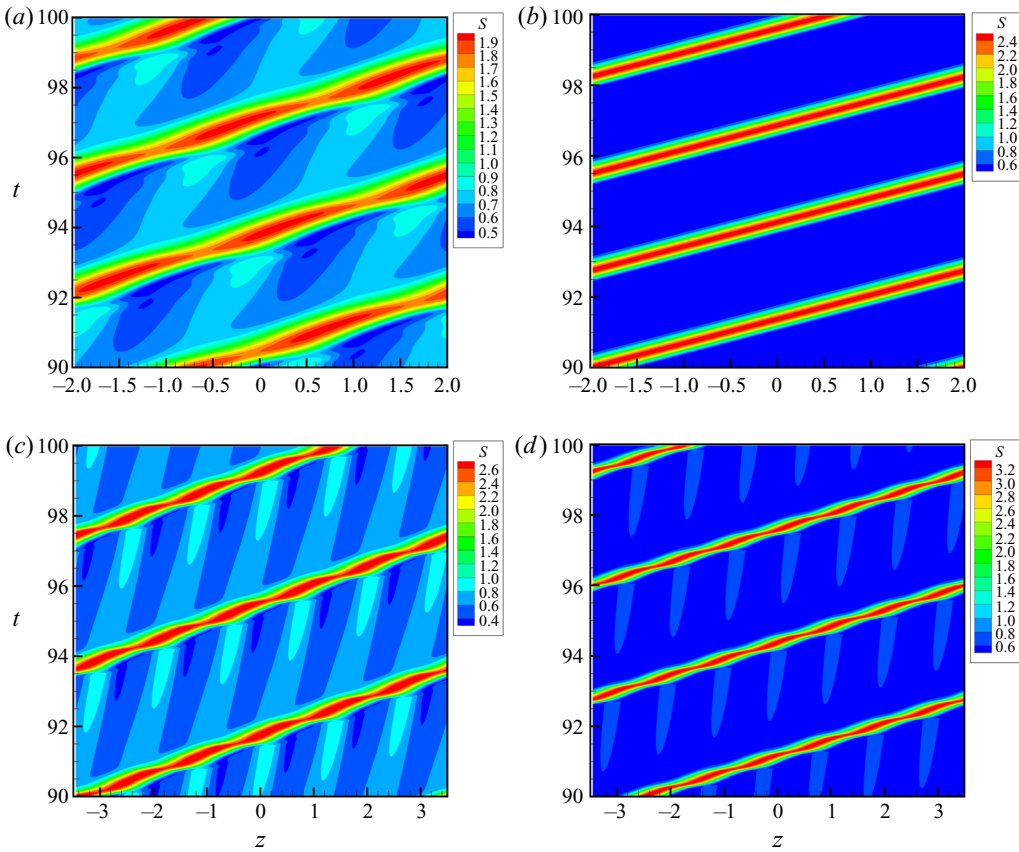


FIGURE 14. The space–time diagrams for the travelling waves perturbed by the most unstable mode. The contours of $S(z, t)$ are marked by different colours. (a) $L = 4$, $\Omega_N = 0$; (b) $L = 4$, $\Omega_N = 0.4$; (c) $L = 7$, $\Omega_N = 0.2$; (d) $L = 7$, $\Omega_N = 0.4$. Other parameters are $\epsilon = 0.2$ and $a = 0.25$.

initial guess of $X_0 = [S_0, s_0, T_0]^T$, we can obtain a better guess $X_0 + \delta X_0$ by solving

$$\frac{\partial F}{\partial S_0} \delta S_0 + \frac{\partial F}{\partial s} \delta s + \frac{\partial F}{\partial T} \delta T = -F, \tag{5.16}$$

where $F = S(z + s, t + T) - S_0$. The solution S_0 is approximated by a Fourier expansion of $2N$ modes. Plus two other unknown parameters T and s , there are $2N + 2$ unknowns. To close the system, we require the update δX_0 has no component in the z direction and the t direction (Ding & Willis 2019):

$$\frac{\partial S_0^T}{\partial z} \delta S_0 = 0, \tag{5.17}$$

$$\frac{\partial S_0^T}{\partial t} \delta S_0 = 0. \tag{5.18}$$

Equation (5.16) and the two constraints constitute the following linear algebra problem:

$$A\delta X = b, \tag{5.19}$$

where $\mathbf{b} = [F, 0, 0]^T$. It is impossible to write down the explicit Jacobian \mathbf{A} but an alternative way to solve this problem is to work in the Krylov subspace spanned by $\mathcal{K}_n = \{\mathbf{b}, \mathbf{A}\mathbf{b}, \mathbf{A}^2\mathbf{b}, \dots, \mathbf{A}^{n-1}\mathbf{b}\}$. To evaluate the result of multiplication by the Jacobian, we use the approximation

$$\frac{\partial S}{\partial S_0} \delta S_0 \approx \frac{S(z, T; S_0 + \varepsilon \delta S_0) - S(z, T; S_0)}{\varepsilon}, \tag{5.20}$$

in which ε is an empirical small parameter and typically $\varepsilon = 10^{-4} \|S_0\| / \|\delta S_0\|$. The generalized minimal residual method (GMRES) iterations are continued until

$$\frac{\| \mathbf{A} \delta \mathbf{X}_n - \mathbf{b} \|}{\| \mathbf{b} \|} \leq tol, \tag{5.21}$$

where tol is the tolerance chosen in the range of 10^{-3} – 10^{-4} . Typically, it takes 10 to 20 GMRES iterations to get a converged solution to $\delta \mathbf{X}_0$. The Newton iteration is terminated when

$$\frac{\|S - S_0\|}{\|S_0\|} \leq 10^{-6}. \tag{5.22}$$

Failure of the Newton iteration is commonplace when the initial guess is poor. To improve the convergence domain, a hookstep method is applied to move $\delta \mathbf{X}_0$ into the trust region. We adapted the Newton–Krylov–hookstep algorithm by Ding & Willis (2019) and implemented the pseudo-arclength continuation technique to it for the present problem. The RPO is tracked from the Hopf bifurcation of the steady travelling-wave solutions, which is continued to other parameters via the pseudo-arclength continuation technique.

In figure 15(a), for $\Omega_N = 0$ the first RPO branch bifurcates from the travelling-wave branch at $l \approx 3.5$, which corresponds to the first unstable mode as shown in figure 12. The bifurcation point of the second RPO branch locates at $l \approx 4.5$. As the parameter $\Omega_N = 0.3$, as shown in figure 15(a), the first RPO branch bifurcates from the travelling-wave branch at $l \approx 4.0$ with $c \approx 1.5$. As shown in figure 15(a), at a given wavelength l , the RPO solution propagates slower than the travelling-wave solution. In this figure, it is found that both the first and the second branches of RPO propagate faster when $\Omega_N = 0.3$. This indicates that rotation can not only promote the mean wave speed of travelling-wave solutions but also the RPO. In figure 15(b), at a given domain size l , the time period of the second RPO solution is obviously smaller than that of the first RPO solution. In figure 15(b), it is found that the value of T of $\Omega_N = 0.3$ is much smaller than the case of $\Omega_N = 0$. The decreasing of the period means that the coalescence and breakup between a large droplet and a small droplet becomes faster. This suggests that the droplet coalescence and breakup process in flow regime ‘c’ can be promoted by the axial rotation.

For higher rotation speed, the travelling waves become more stable due to the rotation as discussed in § 5.2. Thus as Ω_N exceeds a critical value, the RPO branch will disappear because the travelling waves are stable. As shown in figure 16, the first PRO branch is plotted for $\Omega_N = 0.5$. The relation between the RPO branch and the travelling-wave branch is similar to that in figure 15(a). In this figure, the wave speed c of the RPO is closer to that of travelling-wave solution than the cases of lower rotations in figure 15(a). We have not tracked the RPOs at higher rotating speeds because, with the increase of Ω_N , the oscillation becomes weak and the RPOs are very close to the travelling waves.

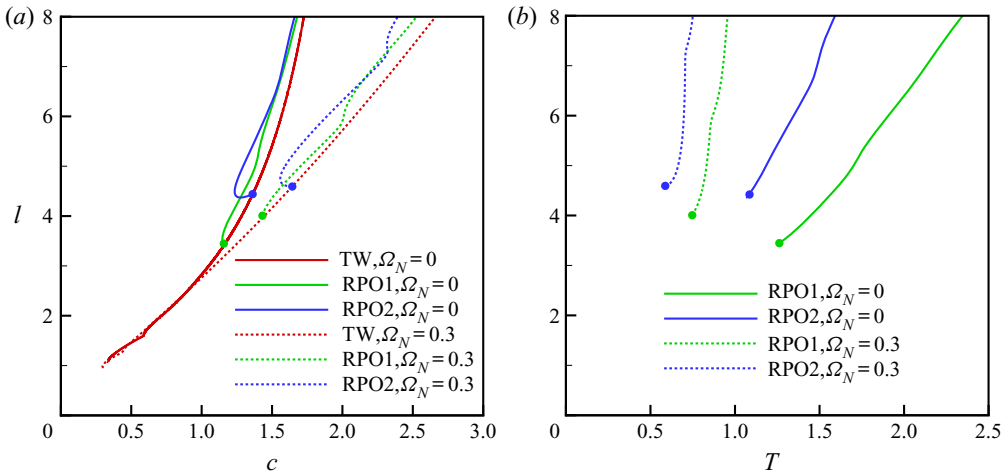


FIGURE 15. (a) The bifurcation diagrams for RPOs in the $c-l$ plane. The propagating speed is defined by $c = s/T$ for RPOs. (b) The curves of the period T versus the domain size l for RPOs. Other parameters are $\epsilon = 0.2$ and $a = 0.25$. The bifurcation points are marked by circles. TW, travelling wave.

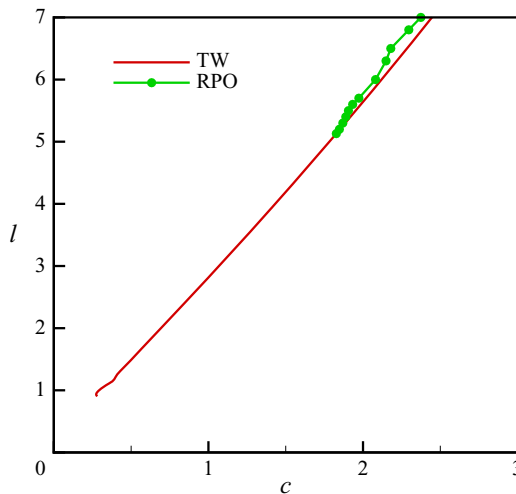


FIGURE 16. The bifurcation diagrams for RPOs in the $c-l$ plane at high rotation with $\Omega_N = 0.5$. Other parameters are $\epsilon = 0.2$ and $a = 0.25$. TW, travelling wave.

6. Summary and conclusions

In the present paper, we have investigated the dynamics of a coating flow driven by gravity over a fibre rotating about its axis. The evolution equation for the surface is derived in the framework of the long-wave theory with an assumption that the characteristic radius of fluid ring is much smaller than the capillary length scale. The parameters a , ϵ and Ω_N are involved in the evolution equation.

A linear stability analysis is performed to examine the influence of rotation on the stability of axisymmetric disturbances. The result of linear stability shows that the rotation is destabilizing without changing the phase speed of the disturbance. The growth rate

and the wavenumber of the most unstable mode, λ_m and k_m , are proportion to $(1 + \Omega_N)^2$ and $(1 + \Omega_N)^{1/2}$, respectively. We also performed a spatio-temporal stability analysis to examine the effect of rotation on the characteristics of the absolute and convective instabilities. The results showed that the increase of Ω_N promotes the absolute instability. The result of the spatio-temporal stability analysis was validated by comparison with numerical simulations on the nonlinear evolution of the long-wave model equation. The results of numerical simulations indicate that with the increase of Ω_N the convectively unstable flow can become absolutely unstable. This result is in excellent agreement with the linear spatio-temporal stability analysis.

The travelling-wave solutions were solved using the Newton method with branch continuation. The effect of rotation on the structure and speed of these solutions was analysed. When the rotation is slow, $\Omega_N < 0.5$, we observed that the travelling-wave speed is promoted by the axial rotation because the height of the droplet becomes larger. However, the travelling-wave speed starts to decrease as the rotation speed increases further because of the strong reversal flow in the wave hump, which retards the motion of droplets.

Linear stability analysis of the travelling-wave solutions was investigated, which showed that the travelling-wave solutions could lose their stabilities to an oscillatory mode when the wavelength exceeds the critical value. With the increase of Ω_N , the travelling-wave solutions become more stable. When the travelling wave is unstable, the disturbance evolves into a near recurrent solution, which was identified as an RPO. We demonstrated that there exists series of RPOs, which are born from the travelling-wave solutions through Hopf bifurcations. Numerical solutions also demonstrate that axial rotation accelerates the mean wave speed of the RPOs and reduce their periods, indicating that axial rotation can promote the droplet coalescence and breakup process in the system.

Acknowledgments

R.L. is supported by The National Natural Science Foundation of China (grant no. 51766002) and The Guangxi Natural Science Foundation (no. 2018GXNSFAA281331). Z.D. is supported by an EPSRC grant optimisation in fluid mechanics EP/P000959/1 and Heilongjiang Touyan Innovation Team Program.

Declaration of interests

The authors report no conflict of interest.

Appendix A. Direct simulations on the evolution of coating flow

In § 2.2, the results of linear stability analysis showed that both the axisymmetric mode and the non-axisymmetric mode with $m = 1$, $k = 0$ can be the most unstable mode. In the appendix, we will perform direct simulations on the nonlinear evolutions on these two cases. For the axisymmetric case, the results of the Navier–Stokes equations are used to validate the long wave model. For the non-axisymmetric case with $m = 1$, $k = 0$, no asymptotic model has been derived for thick films. The nonlinear evolution has to be examined based on the direct simulations.

A.1. Axisymmetric case

For axisymmetric problem, i.e. $\partial_\theta = 0$ for all variables, we introduce the coordinate transformation

$$t = \tilde{t}, \quad z = \tilde{z}, \quad r = h(\tilde{z}, \tilde{t})\tilde{r} + a, \tag{A 1}$$

where the thickness of the film $h(\tilde{z}, \tilde{t}) = S(\tilde{z}, \tilde{t}) - a$. This set of mappings transforms an arbitrarily shaped flow region to a rectangular region. The first-order derivatives read

$$\partial_r = \frac{1}{h}\partial_{\tilde{r}}, \quad \partial_z = \partial_{\tilde{z}} - \frac{\partial_z h}{h}\tilde{r}\partial_{\tilde{r}}, \quad \partial_t = \partial_{\tilde{t}} - \tilde{r}\frac{\partial_{\tilde{t}} h}{h}\partial_{\tilde{r}}, \tag{A 2}$$

and the second-order derivatives read

$$\begin{aligned} \partial_{rr} &= \frac{1}{h^2}\partial_{\tilde{r}\tilde{r}}, \\ \partial_{zz} &= \partial_{\tilde{z}\tilde{z}} + \left[2\left(\frac{\partial_z h}{h}\right)^2 - \frac{\partial_{zz} h}{h} \right]\tilde{r}\partial_{\tilde{r}} - 2\frac{\partial_z h}{h}\tilde{r}\partial_{\tilde{r}\tilde{z}} + \left(\frac{\partial_z h}{h}\right)^2\tilde{r}^2\partial_{\tilde{r}\tilde{r}}. \end{aligned} \tag{A 3}$$

Inserting (A 2) and (A 3) into the Navier–Stokes equations yields

$$\left(\frac{1}{h}\partial_{\tilde{r}} + \frac{1}{r}\right)u + \left(\partial_{\tilde{z}} - \frac{\partial_z h}{h}\tilde{r}\partial_{\tilde{r}}\right)w = 0, \tag{A 4}$$

$$\epsilon^2 Re \left\{ \left(\partial_{\tilde{t}} - \tilde{r}\frac{\partial_{\tilde{t}} h}{h}\partial_{\tilde{r}}\right)u + F_u \right\} = -\epsilon^{-2}\frac{1}{h}\partial_{\tilde{r}}p + \epsilon^{-2}\Omega_N(h\tilde{r} + a) + \left(\Delta - \frac{1}{r^2}\right)u, \tag{A 5}$$

$$\epsilon^2 Re \left\{ \left(\partial_{\tilde{t}} - \tilde{r}\frac{\partial_{\tilde{t}} h}{h}\partial_{\tilde{r}}\right)w + F_w \right\} = 1 - \left(\partial_{\tilde{z}} - \frac{\partial_z h}{h}\tilde{r}\partial_{\tilde{r}}\right)p + \Delta w, \tag{A 6}$$

in which

$$\Delta = \frac{1}{h^2}\partial_{\tilde{r}\tilde{r}} + \frac{1}{rh}\partial_{\tilde{r}} + \epsilon^2 \left\{ \partial_{\tilde{z}\tilde{z}} + \left[2\left(\frac{\partial_z h}{h}\right)^2 - \frac{\partial_{zz} h}{h} \right]\tilde{r}\partial_{\tilde{r}} - 2\frac{\partial_z h}{h}\tilde{r}\partial_{\tilde{r}\tilde{z}} + \left(\frac{\partial_z h}{h}\right)^2\tilde{r}^2\partial_{\tilde{r}\tilde{r}} \right\}, \tag{A 7}$$

and

$$F_u = u\frac{1}{h}\partial_{\tilde{r}}u + w\left(\partial_{\tilde{z}} - \frac{\partial_z h}{h}\tilde{r}\partial_{\tilde{r}}\right)u, \tag{A 8}$$

$$F_w = u\frac{1}{h}\partial_{\tilde{r}}w + w\left(\partial_{\tilde{z}} - \frac{\partial_z h}{h}\tilde{r}\partial_{\tilde{r}}\right)w. \tag{A 9}$$

The boundary conditions at the fibre wall are

$$u = w = 0, \tag{A 10}$$

and at the surface are

$$\begin{aligned} &-\frac{2\epsilon^2}{1 + \epsilon^2(\partial_z S)^2} \left\{ \left[1 + \epsilon^2(\partial_z S)^2 \right] \frac{u}{r} + \partial_z w + \epsilon^2 \partial_z S \partial_z u \right\} \\ &= p - \frac{1}{S \left[1 + \epsilon^2(\partial_z S)^2 \right]^{1/2}} + \frac{\epsilon^2 \partial_{zz} S}{\left[1 + \epsilon^2(\partial_z S)^2 \right]^{3/2}}, \end{aligned} \tag{A 11}$$

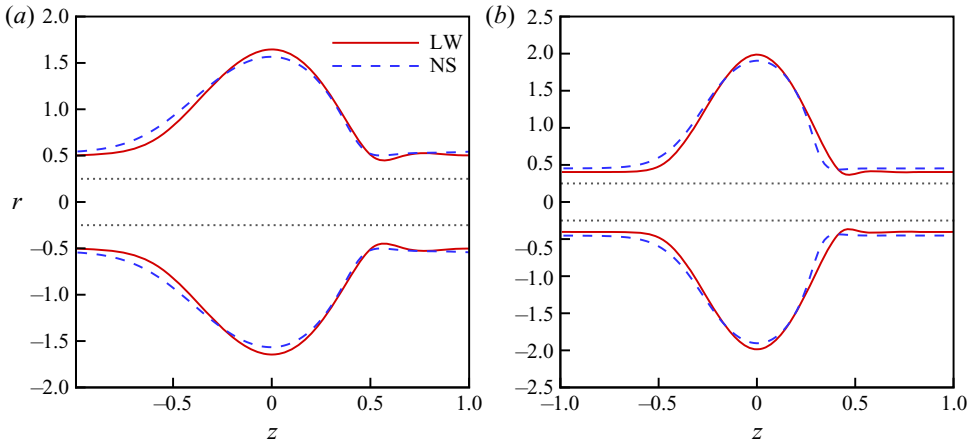


FIGURE 17. The profiles of the interface of the travelling-wave solution of the full Navier–Stokes equations (NS) and the long-wave model (LW). (a) $\Omega_N = 0.0$; (b) $\Omega_N = 0.5$. Other parameters are $\epsilon = 0.2$, $a = 0.25$ and $l = 2$.

$$\frac{[1 + \epsilon^2 (\partial_z S)^2]^2}{h} \partial_r w = \epsilon^2 [3 + \epsilon^2 (\partial_z S)^2] \partial_z S \partial_z w - \epsilon^2 (1 - \epsilon^2 \partial_z S^2) \partial_z u + [1 + \epsilon^2 (\partial_z S)^2] \epsilon^2 \partial_z S \frac{u}{r}, \quad (\text{A } 12)$$

$$\partial_t S^2 + 2 \partial_z \left(\int_a^S wr \, dr \right) = 0. \quad (\text{A } 13)$$

The rectangular domain is discretized by the Fourier–Chebyshev method, grid $[\tilde{z}_1, \tilde{z}_2, \dots, \tilde{z}_M] \times [\tilde{r}_1, \tilde{r}_2, \dots, \tilde{r}_N]$ with M and N mesh points in \tilde{z} and \tilde{r} directions, respectively. The temporal evolution of the problem is obtained by two steps:

$$\left. \begin{aligned} h(\tilde{z}, \tilde{t}) &\rightarrow h(\tilde{z}, \tilde{t} + \delta\tilde{t}), \\ (u, w)(\tilde{z}, \tilde{t}) &\rightarrow (u, w)(\tilde{z}, \tilde{t} + \delta\tilde{t}). \end{aligned} \right\} \quad (\text{A } 14)$$

For more details of the procedure of the time stepping, we refer the readers to the work by Richter & Besthorn (2019) in which an algorithm based on a nonlinear coordinate transformation is used for direct numerical simulations of liquid films under horizontal and vertical external vibrations.

In order to validate our long-wave model, we have compared the travelling-wave solutions of the long-wave model with that of the Navier–Stokes equations for several sets of parameters. The results of the Navier–Stokes equations are the saturated states of the most unstable modes after a long-time evolution. In figure 17, we present the results of these two models for $\Omega_N = 0$ and 0.5. As shown in figure 17(a,b), the profiles of the interface of the long-wave mode are similar to those of the Navier–Stokes equations. In figure 18, we compare the maximum of the position of the interface, S_{max} , of the long-wave model and Navier–Stokes for various Ω_N . As shown in this figure, the results of the long-wave model are in good agreement with those of the Navier–Stokes equations. This means that the long-wave model is valid for the parameters in the present study.

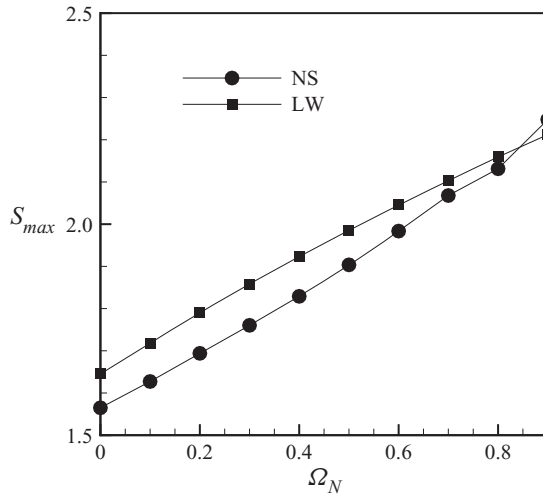


FIGURE 18. The comparison between the travelling-wave solution of the full Navier–Stokes equations (NS) and the long-wave model (LW) for various Ω_N . Other parameters are $\epsilon = 0.2$, $a = 0.25$ and $l = 2$.

A.2. Non-axisymmetric case of $k = 0$

For the non-axisymmetric case of $k = 0$, the flow is streamwise uniform, i.e. $\partial_z = 0$. The controlling equations are expressed as

$$\partial_r u + \frac{u}{r} + \frac{1}{r} \partial_\theta v = 0, \tag{A 15}$$

$$\epsilon^4 Re \left(\partial_t u + u \partial_r u + \frac{v}{r} \partial_\theta u - \frac{v^2}{r} \right) = -\partial_r p + \Omega_N r + \epsilon^2 \left[\partial_{rr} u + \frac{\partial_r u}{r} + \frac{1}{r^2} \partial_{\theta\theta} u - \frac{u}{r^2} \right], \tag{A 16}$$

$$\epsilon^4 Re \left(\partial_t v + u \partial_r v + \frac{v}{r} \partial_\theta v + \frac{uv}{r} \right) = -\frac{1}{r} \partial_\theta p + \epsilon^2 \left[\partial_{rr} v + \frac{\partial_r v}{r} + \frac{1}{r^2} \partial_{\theta\theta} v - \frac{v}{r^2} \right]. \tag{A 17}$$

At the fibre wall ($r = a$), the boundary conditions are

$$u = v = 0. \tag{A 18}$$

At the free surface, the boundary conditions are

$$\left[1 - \left(\frac{\partial_\theta S}{r} \right)^2 \right] \left\{ r \partial_r \left(\frac{v}{r} \right) + \frac{\partial_\theta u}{r} \right\} + 2 \frac{\partial_\theta S}{r} \left(\partial_r u - \frac{\partial_\theta v}{r} - \frac{u}{r} \right) = 0, \tag{A 19}$$

$$-p + 2\epsilon^2 N^{-2} \left\{ \partial_r u - \frac{\partial_\theta S}{r} \left[r \partial_r \left(\frac{v}{r} \right) + \frac{\partial_\theta u}{r} \right] + \left(\frac{\partial_\theta S}{r} \right)^2 \left(\frac{\partial_\theta v}{r} + \frac{u}{r} \right) \right\} = 2H, \tag{A 20}$$

$$S_t + \frac{1}{S} \partial_\theta \int_a^S v \, dr = 0. \tag{A 21}$$

in which the principal curvature

$$2H = -\frac{1}{N} \left\{ \frac{1}{S} + \frac{(\partial_\theta S)^2}{S^3} - \frac{\partial_{\theta\theta} S}{S^2} \right\} - \frac{1}{N^2} \frac{\partial_\theta N \partial_\theta S}{S^2}, \quad (\text{A } 22)$$

where

$$N = \sqrt{1 + r^{-2}(\partial_\theta S)^2}. \quad (\text{A } 23)$$

We introduced the coordinate transformation

$$t = \tilde{t}, \quad \theta = \tilde{\theta}, \quad r = h(\tilde{\theta}, \tilde{t})\tilde{r} + a, \quad (\text{A } 24)$$

where the thickness of the film $h = S(\theta, t) - a$. The first-order derivatives

$$\partial_r = \frac{1}{h} \partial_{\tilde{r}}, \quad \partial_\theta = \partial_{\tilde{\theta}} - \frac{\partial_{\tilde{\theta}} h}{h} \tilde{r} \partial_{\tilde{r}}, \quad \partial_t = \partial_{\tilde{t}} - \tilde{r} \frac{\partial_{\tilde{t}} h}{h} \partial_{\tilde{r}}, \quad (\text{A } 25)$$

and the second-order derivatives

$$\begin{aligned} \partial_{rr} &= \frac{1}{h^2} \partial_{\tilde{r}\tilde{r}}, \\ \partial_{\theta\theta} &= \partial_{\tilde{\theta}\tilde{\theta}} + \left[2 \left(\frac{\partial_{\tilde{\theta}} h}{h} \right)^2 - \frac{\partial_{\tilde{\theta}\tilde{\theta}} h}{h} \right] \tilde{r} \partial_{\tilde{r}} - 2 \frac{\partial_{\tilde{\theta}} h}{h} \tilde{r} \partial_{\tilde{r}\tilde{\theta}} + \left(\frac{\partial_{\tilde{\theta}} h}{h} \right)^2 \tilde{r}^2 \partial_{\tilde{r}\tilde{r}}. \end{aligned} \quad (\text{A } 26)$$

The numerical method for solving the problem is similar to the axisymmetric case.

In the numerical simulations, the initial state is given by

$$S(\theta, 0) = 1 + \delta \cos(\theta), \quad (\text{A } 27)$$

in which δ is a small number. At the initial time, the maximum and the minimum of S locates at $\theta = 0$ and $\theta = \pi$, respectively. Because of the destabilizing effect of rotation, the film thickness increases with time near the region of $\theta = 0$ and the decreases gradually on the opposite side. After a long-time evolution, the film thickness at $\theta = \pi$ approaches zero. This process corresponds to the fluid detachment from the substrate. As the minimum thickness approaches zero, the stiffness of the numerical procedure increases dramatically. In our simulations, we terminate the process of time stepping when the minimum thickness is close to 0.01. In [figure 19](#), we present the profile of the free surface of the evolution of the non-axisymmetric mode with $m = 1$ and $k = 0$ when the film is close to the detachment. As shown in [figure 19\(a\)](#) for $a = 0.8$, the profile of the free surface is close to a circle. However, as shown in [figure 19\(b\)](#) for $a = 0.3$, the profile evolves into a flat lobe due to the destabilizing body force.

The simulations on the disturbance with $m = 1$ and $k = 0$ showed the process of detachment from the substrate. However, these streamwise uniform surface is unstable due to the Rayleigh–Plateau mechanism. We can expect that in the process of detachment, there exists the formation of non-axisymmetric beads. The dynamics of this complex process needs further investigation on the stability analysis of the full linearized Navier–Stokes equations.

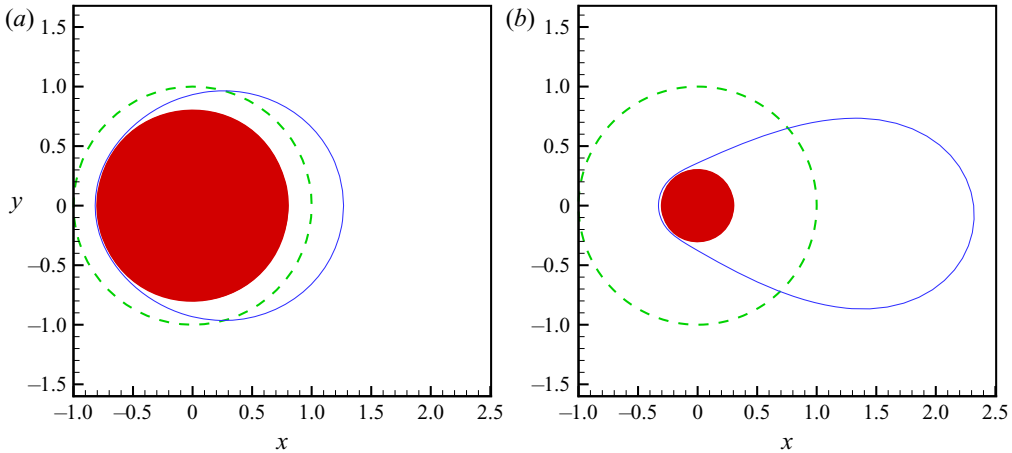


FIGURE 19. The profile of free surface of the evolution of the non-axisymmetric mode with $m = 1$ and $k = 0$. (a) For $a = 0.8$; (b) for $a = 0.3$. The parameters $\epsilon = 0.3$ and $\Omega_N = 0.489$ corresponding to the frequency of rotation $f = 20$.

Appendix B. Thin film model for 3-D evolutions

We introduce the dimensionless variables as follows:

$$(r, z) = a(r^*, z^*), \quad y = Hy^*, \quad t = aV^{-1}t^*, \quad (u, v, w) = V(\epsilon u^*, v^*, w^*), \quad p = \rho g a p^*, \tag{B 1}$$

where the star, $*$, denotes dimensionless variables. A new variable is introduced, $y = r - a$, in the terms related to ∂_r . The aspect ratio $\epsilon = H/a$, the velocity scale $V \equiv \rho g H^2 / \mu$ in which $H = R - a$. We consider the thin film problem in which $\epsilon \ll 1$.

For simplicity, we dropped $*$ for all dimensionless variables. Neglecting the contribution of inertial terms and the higher terms of ϵ The dimensionless nonlinear evolution equation is expressed as

$$S \partial_t S + \partial_\theta Q_\theta + \partial_z Q_z = 0, \tag{B 2}$$

in which

$$Q_\theta = \epsilon^{-2} \partial_\theta p \left\{ \frac{1}{\ln S - 1} + \frac{1}{2} (S^2 + 1) \right\}, \tag{B 3}$$

$$Q_z = \epsilon^{-2} (\partial_z p - 1) \left\{ \frac{(S^2 - 1)(3S^2 - 1)}{16} - \frac{1}{4} S^4 \ln S \right\}, \tag{B 4}$$

$$p = \frac{1}{2} \epsilon^{-1} \Omega'_N (r^2 - S^2) + Ca^{-1} \left[\frac{1}{S} - \frac{\partial_{\theta\theta} S}{S^2} - \partial_{zz} S \right]. \tag{B 5}$$

The parameter $\Omega'_N = a\Omega^2/g$ and $Ca = \rho g a^2 / \sigma$. Note that when discussing the results, we used Ω_N instead of Ω'_N .

The linear stability analysis showed that both axisymmetric and non-axisymmetric disturbance can be the unstable mode. For the nonlinear dynamics in fluid mechanics, many previous studies showed that the transition has non-unique routes, which depend on the initial conditions. In this appendix, we will show that there exists different routes of evolutions for various rotation parameters.

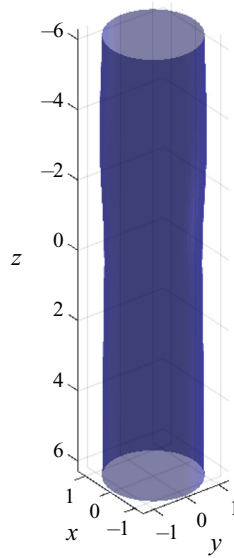


FIGURE 20. The profile of the surface at the saturated state for the case at $\Omega_N = 0.122$, $\epsilon = 0.3$. The dimensional parameters are $a = 0.8$ mm and the thickness is $H = 0.2$ mm.

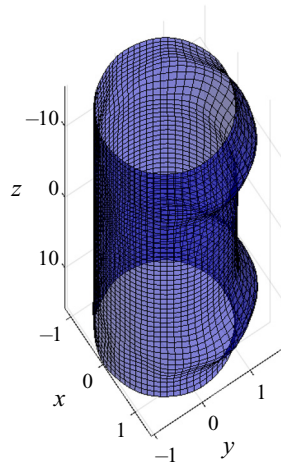


FIGURE 21. The profile of the surface at the saturated state for the case at $\Omega_N = 0.5$, $\epsilon = 0.3$. The dimensional parameters are $a = 0.8$ mm and the thickness is $H = 0.2$ mm.

Firstly, we study the case of a small rotation number. We choose the parameters $\Omega_N = 0.122$ and $\epsilon = 0.3$ as in figure 2. For a non-axisymmetric initial condition (there is no streamwise component), $h = 1 + \delta \sin(\theta)$ or $h = 1 + \delta \sin(\theta + kz)$, the flow is unstable and a non-axisymmetric and a streamwise uniform state can develop. But if there is a streamwise component (we set $h = 1 + \delta \sin(\theta) + \delta \sin(kz)$), we observe that the final state is axisymmetric which indicates that the non-axisymmetric mode is suppressed by the axisymmetric mode (see figure 20). This study indicates that the axisymmetric state will be observed in experiments when the rotation is slow, because the axisymmetric mode is the most unstable and grows fastest.

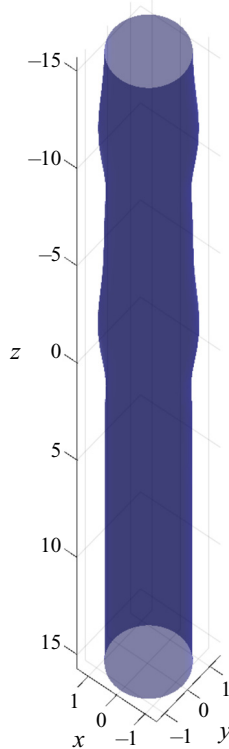


FIGURE 22. The profile of the surface at the saturated state for the case at $\Omega_N = 0.5$, $\epsilon = 0.3$. The dimensional parameters are $a = 0.8$ mm and the thickness is $H = 0.2$ mm. Here we perturbed the saturated axisymmetric state by a non-axisymmetric disturbance.

We also studied the case of a large rotation number. We choose $\Omega_N = 0.5$ and $\epsilon = 0.3$ as in figure 2. We tested two different initial conditions, $h = 1 + \delta \sin(\theta) + \delta \sin(kz)$ and $h = 1 + \delta \sin(kz)$. For the axisymmetric initial condition, we observe that the state remains axisymmetric. However, as expected, a 3-D state develops when the system is perturbed by the non-axisymmetric initial condition (see figure 21). However, if we rotate the cylinder after the formation of axisymmetric beads (or perturb the saturated axisymmetric state by non-axisymmetric disturbances), we did observe that the system reverts back to the axisymmetric state in the parametric space considered in the present study (see figure 22). This demonstrates that we may observe an axisymmetric film in experiments if we gradually increase the rotation speed or rotate the cylinder after the formation of axisymmetric beads.

REFERENCES

- ASHMORE, J. & HOSOI, A. E. 2003 The effect of surface tension on rimming flows in a partially filled rotating cylinder. *J. Fluid Mech.* **479**, 65–98.
- BENILOV, E. S. & LAPIN, V. N. 2013 Inertial instability of flows on the inside or outside of a rotating horizontal cylinder. *J. Fluid Mech.* **736**, 107–129.
- BERS, A. 1975 Linear waves and instabilities. In *Physique des Plasmas* (ed. C. DeWitt & J. Peyraud). Gordon & Breach.

- BLYTH, M. G., TSELUIKO, D., LIN, T.-S. & KALLIADASIS, S. 2018 Two-dimensional pulse dynamics and the formation of bound states on electrified falling films. *J. Fluid Mech.* **885**, 210–235.
- BRIGGS, R. J. 1964 *Electron-Stream Interaction with Plasmas*. MIT.
- CHANDLER, G. J. & KERSWELL, R. R. 2013 Invariant recurrent solutions embedded in a turbulent two-dimensional Kolmogorov flow. *J. Fluid Mech.* **722**, 554–595.
- CHANG, H.-C. & DEMEKHIN, E. A. 1999 Mechanism for drop formation on a coated vertical fibre. *J. Fluid Mech.* **380**, 233–255.
- CHAROGIANNIS, A., DENNER, F., VAN WACHEM, B. G., KALLIADASIS, S., SCHEID, B. & MARKIDES, C. N. 2018 Experimental investigations of liquid falling films flowing under an inclined planar substrate. *Phys. Rev. Fluids* **3** (11), 114002.
- CHEN, C. I., CHEN, C. K. & YANG, Y. T. 2004 Perturbation analysis to the nonlinear stability characterization of thin condensate falling film on the outer surface of a rotating vertical cylinder. *Int. J. Heat Mass Transfer* **47**, 1937–1951.
- CRASTER, R. V. & MATAR, O. K. 2006 On viscous beads flowing down a vertical fibre. *J. Fluid Mech.* **553**, 85–105.
- CVITANOVIĆ, P., ARTUSO, R., MAINIERI, R., TANNER, G. & VATTAY, G. 2018 *Chaos: Classical and Quantum*, 16.0th edn. ChaosBook.org.
- DÁVALOS-OROZCO, L. A. & RUIZ-CHAVARRÍA, G. 1993 Hydrodynamic instability of a fluid layer flowing down a rotating cylinder. *Phys. Fluids A* **5** (10), 2390–2404.
- DIETZE, G. F. & RUYER-QUIL, C. 2015 Films in narrow tubes. *J. Fluid Mech.* **762**, 68–109.
- DING, Z. & WILLIS, A. P. 2019 Relative periodic solutions in conducting liquid films flowing down vertical fibres. *J. Fluid Mech.* **873**, 835–855.
- DUPRAT, C., GIORGIUTTI-DAUPHINÉ, F., KALLIADASIS, S. & GIORGIUTTI-DAUPHINÉ, F. 2009 Liquid film coating a fiber as a model system for the formation of bound states in active dispersive-dissipative nonlinear media. *Phys. Rev. Lett.* **82**, 244502.
- DUPRAT, C., RUYER-QUIL, C., KALLIADASIS, S. & GIORGIUTTI-DAUPHINÉ, F. 2007 Absolute and convective instabilities of a viscous film flowing down a vertical fiber. *Phys. Rev. Lett.* **82**, 244502.
- EGGERS, J. & DUPONT, T. F. 1994 Drop formation in a one-dimensional approximation of the Navier–Stokes equation. *J. Fluid Mech.* **262**, 205–221.
- FRENKEL, A. L. 1992 Nonlinear theory of strongly undulating thin films flowing down vertical cylinders. *Europhys. Lett.* **18** (7), 583–588.
- GROH, C. M. & KELMANSON, M. A. 2014 Inertially induced cyclic solutions in thin-film free-surface flows. *J. Fluid Mech.* **755**, 628–653.
- HALPERN, D. & WEI, H.-H. 2017 Slip-enhanced drop formation in a liquid falling down a vertical fibre. *J. Fluid Mech.* **820**, 42–60.
- HOSOI, A. E. & MAHADEVAN, L. 1999 Axial instability of a free-surface front in a partially filled horizontal cylinder. *Phys. Fluids* **11**, 97–106.
- HUERRE, P. & MONKEWITZ, P. A. 1990 Local and global instabilities in spatially developing flows. *Annu. Rev. Fluid Mech.* **22**, 473–537.
- JI, H., FALCON, C., SADEGHPOUR, A., ZENG, Z., JU, Y. S. & BERTOZZI, A. L. 2019 Dynamics of thin liquid films on vertical cylindrical fibres. *J. Fluid Mech.* **865**, 303–327.
- JOHNSON, R. E. 1988 Steady-state coating flows inside a rotating horizontal cylinder. *J. Fluid Mech.* **190**, 321–342.
- KALLIADASIS, S. & CHANG, H.-C. 1994 Drop formation during coating of vertical fibres. *J. Fluid Mech.* **261**, 135–168.
- KALLIADASIS, S., RUYER-QUIL, C., SCHEID, B. & VELARDE, M. G. 2012 *Falling Liquid Films*. Springer.
- KAPITZA, P. L. & KAPITZA, S. P. 1949 Wave flow of thin viscous liquid films. III. Experimental study of wave regime of a flow. *J. Exp. Theor. Phys.* **19** (2), 105–120.
- KERCHMAN, V. I. & FRENKEL, A. L. 1994 Interactions of coherent structures in a film flow: simulations of a highly nonlinear evolution equation. *Theor. Comput. Fluid Dyn.* **6**, 235–254.
- KLIAKHANDLER, I. L., DAVIS, S. H. & BANKOFF, S. G. 2001 Viscous beads on vertical fibre. *J. Fluid Mech.* **429**, 381–390.
- LIU, J. & GOLLUB, J. P. 1994 Solitary wave dynamics of film flows. *Phys. Fluids* **6** (5), 1702–1712.

- LIU, R. & LIU, Q. S. 2014 Thermocapillary effect on the dynamics of viscous beads on vertical fiber. *Phys. Rev. E* **90**, 033005.
- LOPES, A. V. B., THIELE, U. & HAZEL, A. L. 2018 On the multiple solutions of coating and rimming flows on rotating cylinders. *J. Fluid Mech.* **835**, 540–574.
- MOFFATT, H. K. 1977 Behaviour of a viscous film on the outer surface of a rotating cylinder. *J. Méc.* **16**, 651–673.
- NOSOKO, T. & MIYARA, A. 2004 The evolution and subsequent dynamics of waves on a vertically falling liquid film. *Phys. Fluids* **16** (4), 1118–1126.
- POUGATCH, K. & FRIGAARD, I. 2011 Thin film flow on the inside surface of a horizontally rotating cylinder: steady state solutions and their stability. *Phys. Fluids* **23**, 022102.
- QUÉRÉ, D. 1990 Thin films flowing on vertical fibers. *Europhys. Lett.* **13** (8), 347–384.
- QUÉRÉ, D. 1999 Fluid coating on a fiber. *Annu. Rev. Fluid Mech.* **31**, 347–384.
- RAYLEIGH, LORD 1892 On the instability of a cylinder of viscous liquid under capillary force. *Phil. Mag.* **34**, 145–154.
- RICHTER, S. & BESTEHORN, M. 2019 Direct numerical simulations of liquid films in two dimensions under horizontal and vertical external vibrations. *Phys. Rev. Fluids* **4**, 044004.
- RIETZ, M., SCHEID, B., GALLAIRE, F., KOFMAN, N., KNEER, R. & ROHLFS, W. 2017 Dynamics of falling films on the outside of a vertical rotating cylinder: waves, rivulets and dripping transitions. *J. Fluid Mech.* **832**, 189–211.
- RUSCHAK, K. J. & SCRIVEN, L. E. 1976 Rimming flow of liquid in a rotating horizontal cylinder. *J. Fluid Mech.* **76**, 113–125.
- RUYER-QUIL, C., TREVELEYAN, P., GIORGIUTTI-DAUPHINÉ, F., DUPAT, C. & KALLIADASIS, S. 2008 Modelling film flows down a fibre. *J. Fluid Mech.* **603**, 431–462.
- SADEGHPOUR, A., ZENG, Z., JI, H., EBRAHIMI, N. D., BERTOZZI, A. L. & JU, Y. S. 2019 Water vapor capturing using an array of travelling liquid beads for desalination and water treatment. *Sci. Adv.* **5**, eaav7662.
- SHLAG, T. & SIVASHINSKY, G. I. 1982 Irregular flow of a liquid film down a vertical column. *J. Phys. (Paris)* **43**, 459–466.
- SNOEIJER, J. H. 2006 Free-surface flows with large slopes: beyond lubrication theory. *Phys. Fluids* **18**, 021701.
- THORODDSEN, S. T. & MAHADEVAN, L. 1997 Experimental studies of the instabilities in a partially filled horizontal rotating cylinder. *Exps. Fluids* **23**, 1–13.